Iron Force Constants of Bridgmanite at High Pressure: Implications for Iron Isotope Fractionation in the Deep Mantle

Wenzhong Wang[1,2*], Jiachao Liu[3,4], Hong Yang[5†], Susannah M. Dorfman[4,*], Mingda Lv[4], Jie Li[6], Feng Zhu[6], Jiyong Zhao[7], Michael Y. Hu[7], Wenli Bi[7,8], Ercan E. Alp[7], Yuming Xiao[9], Zhongqing Wu[1,*], Jung-Fu Lin[3,*]

[1]Laboratory of Seismology and Physics of Earth's Interior, School of Earth and Space Sciences, University of Science and Technology of China, Hefei, China;

[2]Department of Earth Sciences, University College London, Gower Street, London WC1E 6BT, UK;

[3]Department of Geological Sciences, Jackson School of Geosciences, The University of Texas at Austin, Austin, Texas 78712, USA;

[4]Department of Earth and Environmental Sciences, Michigan State University, MI 48824, USA

[5]Center for High Pressure Science and Technology Advanced Research (HPSTAR), Pudong, Shanghai 201203, China;

[6]Department of Earth and Environmental Sciences, University of Michigan, MI 48109, USA;

[7]Advanced Photon Source, Argonne National Laboratory, Argonne, Illinois 60439, USA;

[8]Department of Geology, University of Illinois at Urbana-Champaign, Urbana, Illinois 61801, USA;

[9]High Pressure Collaborative Access Team (HPCAT), X-Ray Science Division, Argonne National Lab, Argonne, Illinois 60439, USA;

[†] Now at Department of Geological Sciences, Stanford University, Stanford, CA 94305, USA.

[*] J.C. Liu and W.Z. Wang contributed equally to this work.

Corresponding authors: W. Wang (wenzhong.wang@ucl.ac.uk), S. M. Dorfman (dorfman3@msu.edu), J.F. Lin (afu@jsg.utexas.edu), or Zhongqing Wu (wuzq10@ustc.edu.cn)

Abstract

The isotopic compositions of iron in major mantle minerals may record chemical exchange between deep-Earth reservoirs as a result of early differentiation and ongoing plate tectonics processes. Bridgmanite (Bdg), the most abundant mineral in the Earth's lower mantle, can incorporate not only Al but also Fe with different oxidation states and spin states, which in turn can influence the distribution of Fe isotopes between Bdg and ferropericlase (Fp) and between the lower mantle and the core. In this study, we combined first-principles calculations with high-pressure nuclear resonant inelastic X-ray scattering measurements to evaluate the effects of Fe site occupancy, valence, and spin states at lower-mantle conditions on the reduced Fe partition function ratio (β-factor) of Bdg. Our results show that the spin transition of octahedral-site (B-site) Fe^{3+} in Bdg under mid-lower-mantle conditions generates a +0.09‰ increase in its β-factor, which is the most significant effect compared to Fe site occupancy and valence. Fe^{2+}-bearing Bdg varieties have smaller β-factor relative to Fe^{3+}-bearing varieties, especially those containing B-site Fe^{3+}. Our models suggest that Fe isotopic fractionation between Bdg and Fp is only significant in the lowermost mantle due to the occurrence of low-spin Fe^{2+} in Fp. Assuming early segregation of an iron core from a deep magma ocean, we find that neither core formation nor magma ocean crystallization would have resulted in resolvable Fe isotope fractionation. In contrast, Fe isotopic fractionation between low-spin Fe^{3+}-bearing Bdg/Fe^{2+}-bearing Fp and metallic iron at the core-mantle boundary may have enriched the lowermost mantle in heavy Fe isotopes by up to +0.20‰.

Keywords: Fe isotopic fractionation, bridgmanite, spin transition, nuclear resonant spectroscopy, first-principles calculations

1. Introduction

Iron, the most abundant element in the Earth by weight, is the dominant component of the core and the only major transition metal in the mantle. Signatures of planetary accretion and differentiation may be recorded in the Fe isotopic compositions ($\delta^{i}Fe=((^{i}Fe/^{54}Fe)_{sample}/(^{i}Fe/^{54}Fe)_{standard}$ - 1)*1000 ‰, i=56 or 57) in the Earth's crust, mantle, and core (Poitrasson et al., 2009; Polyakov, 2009; Poitrasson et al., 2013; Rubie

et al., 2015; Sossi et al., 2016; Elardo and Shahar, 2017; Teng et al., 2017). Terrestrial mid-ocean ridge basalts (MORBs) exhibit strikingly high δ^{56}Fe of 0.105 ± 0.006‰ (Teng et al., 2013) relative to chondritic values, suggesting the enrichment of heavy Fe isotopes in the Earth's upper mantle. Several hypotheses have been proposed to explain the Fe isotope signatures in the mantle, including evaporation loss of light iron isotopes during Earth's accretion (Poitrasson et al., 2004; Poitrasson, 2007), Fe isotopic fractionation during core formation (Polyakov, 2009; Elardo and Shahar, 2017), and mantle partial melting (Teng et al., 2008; Dauphas et al., 2014). Evaluation of the effects of these processes on the Fe isotope composition requires Fe equilibrium isotopic fractionation factors (Δ^{56}Fe) between major Fe-bearing mantle and core minerals/melts under pressure-temperature (P-T) conditions relevant to the early and current Earth's interior.

Bridgmanite (Bdg) and ferropericlase (Fp) are the most abundant Fe-bearing minerals in the lower mantle. As such, the reduced Fe partition function ratios (β-factors) for Bdg, Fp, and iron-light element alloys are key parameters for modelling Fe isotopic fractionation between different minerals/melts in the lower mantle or between the mantle and the core. Generally, β-factors are directly controlled by bond stiffnesses in structures, which in turn depend on structural response to pressure, temperature, and composition (Schauble, 2011; Huang et al., 2013; Huang et al., 2014; Wu et al., 2015a; Shahar et al., 2016; Liu et al., 2017; Yang et al., 2019). In addition, Fe in both Bdg and Fp have been found to undergo spin transitions under mid-lower-mantle conditions (e.g., Lin et al., 2013; Liu et al., 2018), which can significantly change their electronic structures (Hsu et al., 2011), Fe bond stiffnesses (Polyakov, 2009; Rustad and Yin, 2009; Lin et al., 2013), and hence presumably influence Fe isotope fractionation. A recent work conducted by Yang et al. (2019) observed a significant increase in the β-factor of Fp across its Fe^{2+} spin transition in the octahedral site at ~ 60 GPa and 300 K, whereas the β-factor of Bdg remains unchanged with increasing pressure likely due to lattice distortion. Additionally, the effects of light elements on the β-factor of metallic Fe alloy at high P-T conditions will also affect our understanding of deep-Earth iron isotope distribution (Chen et al., 2014; Shahar et al., 2016; Liu et al., 2017; Chen et al., 2018).

The pressure-dependence of the β-factor of Bdg can be very complex when

considering the two possible crystallographic sites can accommodate Fe with different valences and spin states as well as other minor cations like Al. The individual contribution of each lattice site to the mean force constant of the phase cannot be uniquely determined in high-pressure nuclear resonant inelastic X-ray scattering measurements (e.g., Yang et al. 2019) which yields only the total average inelastic scattering behavior of the sample. The Bdg structure accommodates Fe in both the larger pseudo-dodecahedral (8-fold) A-site and the smaller octahedral (6-fold) B-site (Lin et al., 2013). While Fe^{2+} can only reside in the large A-site, Fe^{3+} can enter both sites through different proposed substitution mechanisms such as $Mg^{2+}_A+Si^{4+}_B \rightarrow Fe^{3+}_A+Fe^{3+}_B$ and $Mg^{2+}_A+Si^{4+}_B \rightarrow Fe^{3+}_A+Al^{3+}_B$ (Frost et al., 2004; Liu et al., 2015). Only Fe^{3+} in the Bdg B-site is expected to undergo a high-spin (HS) to low-spin (LS) transition at pressures corresponding to mid-mantle depths, while A-site Fe^{2+} and Fe^{3+} experience lattice distortion but both valence states maintain HS state throughout the lower mantle (Catalli et al., 2010; Hsu et al., 2011; Mao et al., 2015; Shukla and Wentzcovitch, 2016; Fu et al., 2018b; Liu et al., 2018).

Many previous studies have argued that iron exists predominantly as Fe^{3+} in Bdg, on the basis of increased stability of Fe^{3+} in Bdg structure at lower-mantle-relevant oxygen fugacity conditions (Catalli et al., 2010; Frost et al., 2004; Frost and McCammon, 2008; Li et al., 2006; Marquardt et al., 2009; McCammon, 1997). Furthermore, a recent work (Armstrong et al., 2019) also found that Fe^{2+} in a deep magma ocean would disproportionate to Fe^{3+} plus metallic iron at high pressures. As such, consequent segregation of precipitated iron metal from the lower mantle into the core could leave the Bdg enriched in Fe^{3+} after magma ocean crystallization. In addition, experimental studies (Frost et al., 2004; Shim et al., 2017; Andrault et al., 2018) also reporeted Fe^{3+}-rich Bdg in equilibrium with iron metal due to the disproportionation of Fe^{2+}. Although recent experimental and theoretical studies have reported the β-factors of several Bdg compositions (Shahar et al., 2016; Yang et al., 2019), none of the studies have examined the effect of Fe^{3+} in the B-site, precluding the evaluation of the influence of the B-site Fe^{3+} spin transition on the β-factors of Bdg. In addition to Fe^{3+}, Al^{3+} can also enter A and B sites in Bdg through the coupled substitution mechanism $Mg^{2+}_A + Si^{4+}_B = (Fe^{3+}, Al^{3+})_A + (Fe^{3+}, Al^{3+})_B$ (Frost et al., 2004; Liu et al., 2015; Shim et al.,

2017; Yang et al., 2019). As the radius of Al^{3+} is smaller than both A-site and B-site Fe^{3+}, it prefers to substitute into the smaller B-site and the content of B-site Fe^{3+} is influenced by the Fe^{3+}/Al ratio (Frost et al., 2004; Liu et al., 2015; Shim et al., 2017). Thus, comparison of the β-factors between Al-bearing and Al-free Bdg is needed to reveal the effect of Al on the β-factor of Bdg.

In this study, we determine the β-factors of $(Mg_{0.5}Fe^{3+}_{0.5})(Si_{0.5}Fe^{3+}_{0.5})O_3$ Bdg at mantle-relevant pressures by both nuclear resonant inelastic X-ray scattering (NRIXS) and the density functional theory (DFT) augmented by a Hubbard U correction method. The spin transition of the B-site Fe^{3+} in $(Mg_{0.5}Fe^{3+}_{0.5})(Si_{0.5}Fe^{3+}_{0.5})O_3$ Bdg at 43-50 GPa has been inferred from X-ray diffraction, X-ray emission and electrical conductivity measurements (Liu et al., 2018). This sample thus offers the possibility to unambiguously determine the influence of the B-site Fe^{3+} spin transition on its β-factor. In addition, the pressure- and temperature-dependent β-factors of Fe in four other bridgmanite compositions were calculated by the DFT+U method, including Fe^{3+}- and Al^{3+}-bearing Bdg, $(Mg_{0.9375}Fe^{3+}_{0.0625})(Si_{0.9375}Al_{0.0625})O_3$, $(Mg_{0.75}Fe^{3+}_{0.25})(Si_{0.75}Al_{0.25})O_3$, and Fe^{2+}-bearing Bdg, $(Mg_{0.75}Fe^{2+}_{0.25})SiO_3$ and $(Mg_{0.5}Fe^{2+}_{0.5})SiO_3$. The calculated results are used to constrain the effects of valence, spin states, and site occupancies of Fe in Bdg on its β-factor at high pressure and temperature. To assess how Fe isotopes distribute between Bdg and Fp in the lower mantle, our results are further used to model the depth-dependence of $\Delta^{56}Fe_{Bdg\text{-}Fp}$ for various bulk mantle compositions. Finally, we estimate the effect of Fe species in Bdg, Fp, and metallic iron-light element alloys on the scale of Fe isotopic fractionation between the lower mantle and the core.

2. Materials and Methods

2.1. Bridgmanite sample synthesis and DAC preparation

^{57}Fe-enriched $(Mg_{0.46}Fe^{3+}_{0.53})(Si_{0.49}Fe^{3+}_{0.51})O_3$ Bdg sample was synthesized as in Liu et al. (2018). Briefly, fine-powdered 94.45% ^{57}Fe-enriched Fe_2O_3 (Cambridge Isotope Laboratories) was homogeneously mixed with MgO and SiO_2 in 1:1:1 molar ratios. $(Mg_{0.46}Fe^{3+}_{0.53})(Si_{0.49}Fe^{3+}_{0.51})O_3$ akimotoite was recovered from the multi-anvil synthesis at 24 GPa and 1873 K for ~ 9 hours. The sample used in this study is from the same multi-anvil press synthesis used in Liu et al. (2018) and (Dorfman et al. (2020).

Multiple experimental runs confirmed via refinement of X-ray diffraction data that this akimotoite reproducibly and reversibly transforms to Bdg at ~24 GPa and 300 K (Dorfman et al. 2018), therefore the NRIXS measurements collected at 32.5 GPa and above are within the stability field of Bdg. Synchrotron Mössbauer spectroscopy (Liu et al., 2018) and conventional Mössbauer spectroscopy (Dorfman et al., 2020) confirm that all Fe in this sample is Fe^{3+}, which enters Bdg structure through coupled substitution ($Mg^{2+}_A + Si^{4+}_B = Fe^{3+}_A + Fe^{3+}_B$).

A panoramic diamond anvil cell (DAC) equipped with a pair of 300-μm culet diamonds was used for NRIXS measurements up to 60.9 GPa. NRIXS signals at higher pressures were measured from a three-opening panoramic DAC equipped with a pair of 150-μm culet diamonds and three APD detectors at Argonne National Laboratory. To increase the signal-to-background ratio, the upstream diamond was partially perforated to reduce scattering of the incoming X-ray beam. X-ray transparent, high-purity Be gaskets 3 mm in diameter with cubic boron nitride (c-BN) inserts were used to support sample chamber and provide windows for NRIXS signal collection. The c-BN insert was preindented to ~30-μm thickness before a ~70-μm-diameter sample chamber was drilled on its center. In the sample chamber, ~15×15×10 μm^3 sample was sandwiched between two layers of ~5-μm-thick NaCl pressure medium. 5-μm ruby spheres next to the samples were used as pressure gauge (Mao et al., 1986) below ~ 70 GPa. For higher pressure experiments, pressures were determined from the edge of the diamond Raman peak measured at the sample position (Akahama and Kawamura, 2010).

2.2. NRIXS measurements and data analysis

NRIXS measurements for ^{57}Fe-enriched $(Mg_{0.46}Fe^{3+}_{0.53})(Si_{0.49}Fe^{3+}_{0.51})O_3$ Bdg sample (Fig. 1) at 32.5-60.9 GPa and 71.4-101.4 GPa were conducted at beamlines 16-ID-D and 3-ID-B of the Advanced Photon Source, Argonne National Laboratory, respectively. At both beamlines the incident X-ray beam was focused to ~10 μm in diameter on the sample in a DAC. NRIXS spectra were collected by avalanche photo diode (APD) detectors attached to DACs, respectively. Each NRIXS spectrum was generated by scanning energy near the ^{57}Fe nuclear transition energy of 14.4125 keV by tuning a high-resolution monochromator. The energy resolution was 1 meV with a

step size of 0.334 meV at beamline 3-IDB and 2 meV with a step size of 0.67 meV at beamline 16-ID-D. Collection times were 3-5 s/step, for a total of ~1 hour per NRIXS spectrum. At each pressure, 15-40 NRIXS spectra were collected and summed to make sufficient signal-to-noise ratio (Fig. 1). The spectra at pressure below 60.9 GPa were collected at 16 IDD while others were collected at 3-ID-B. The ranges of scanned energy for each spectrum can be found in Fig. 1. These wide energy ranges are critical for capturing the multi-phonon contributions to PDOS and reliable background removal (Dauphas et al., 2018).

NRIXS data were processed using the software package *SciPhon* (Dauphas et al., 2018). First the energy resolution function of the incident X-ray was used to deconvolute the NRIXS spectrum and a linear background based on high-energy (beyond ±100 meV) part of the spectrum was subtracted. The NRIXS spectrum was then used to derive the phonon density of states (PDOS) of iron atoms in the lattice. This derivation uses the harmonic approximation, which assumes the lattice potentials are proportional to atomic displacement squared.

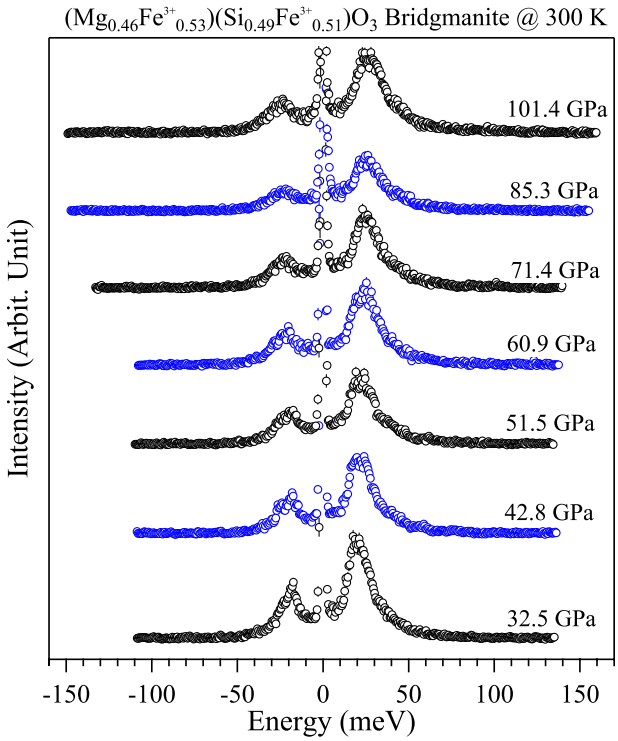

Figure 1. NRIXS spectra of ^{57}Fe-enriched $(Mg_{0.5}Fe^{3+}_{0.5})(Si_{0.5}Fe^{3+}_{0.5})O_3$ bridgmanite sample at 300 K and high pressures. The peak at 0 meV corresponds to the recoilless elastic scattering, while the other inelastic peaks origin from either phonon creation (E > 0) or annihilation (E <

0).

2.3. First-principles calculations

All calculations were performed using the Quantum Espresso package (Giannozzi et al., 2009) based on density functional theory (DFT), plane wave, and pseudopotential. The local density approximation (LDA) was adopted for the exchange correlation function. The energy cutoff for plane waves was 70 Ry. The pseudopotentials for Mg, Si, O, and Al were well described in our previous studies (Huang et al., 2013; Huang et al., 2014; Wu et al., 2015a; Wang and Wu, 2018). The pseudopotential for Fe was generated using the Vanderbilt method (Vanderbilt, 1990) with a valence configuration of $3s^2 3p^6 3d^{6.5} 4s^1 4p^0$ and a cutoff radius of 1.8 Bohr. These pseudopotentials have been successfully applied to predict the structures, vibrational properties, elasticity, and equilibrium isotope fractionation of mantle silicate minerals including bridgmanite in our previous studies (Núñez Valdez et al., 2012; Núñez-Valdez et al., 2013; Huang et al., 2013; Huang et al., 2014; Feng et al., 2014; Wu et al., 2015b; Shukla et al., 2015; Wang et al., 2017a; Wang et al., 2017b; Qian et al., 2018; Wang et al., 2019a). To address the large on-site Coulomb interactions among the localized electrons (Fe 3d electrons) (Anisimov et al., 1991), we introduced a Hubbard *U* correction to the LDA (LDA+*U*) for all DFT calculations. *U* values for Fe^{2+} and Fe^{3+} on A- and/or B- sites in bridgmanite are obtained from previous work (Hsu et al., 2010; Hsu et al., 2011), in which values were non-empirically determined using linear response method (Cococcioni and de Gironcoli, 2005). The U values for A-site Fe^{2+}, A-site HS Fe^{3+}, B-site HS Fe^{3+}, B-site LS Fe^{3+} are 3.1 eV, 3.7 eV, 3.3 eV, and 4.9 eV, respectively. The LDA+U method has been widely and successfully applied to predict the physical and chemical properties of Fe-bearing Bdg and Fp (Hsu et al., 2011; Wu et al., 2013; Shukla and Wentzcovitch, 2016). For $(Mg_{0.5}Fe^{3+}_{0.5})(Si_{0.5}Fe^{3+}_{0.5})O_3$ $(Mg_{0.9375}Fe^{3+}_{0.0625})(Si_{0.9375}Al_{0.0625})O_3$, and $(Mg_{0.75}Fe^{3+}_{0.25})(Si_{0.75}Al_{0.25})O_3$ Bdg, we consider only configurations with the nearest neighbor $[Fe^{3+}]_{Mg}$-$[Fe^{3+}/Al^{3+}]_{Si}$ since they are the lowest energy configurations (Hsu et al., 2011; Shukla and Wentzcovitch, 2016). Crystal structures at variable pressures were optimized on a 6×6×4 k-point mesh, and vibrational density of states (VDOS) were calculated using the finite displacement

method as implemented in the code PHONOPYT (Togo and Tanaka, 2015). At static conditions, the B-site Fe^{3+} undergoes a HS-LS transition at ~52 GPa, consistent with previous LDA+U calculations (Shukla and Wentzcovitch, 2016). This value is ~8 GPa larger than the spin-transition pressure in $(Mg_{0.875}Fe^{3+}_{0.125})(Si_{0.875}Fe^{3+}_{0.125})O_3$ Bdg due to the difference in Fe^{3+} content.

Reduced partition function ratios were computed from phonon frequencies obtained from DFT calculations. The reduced partition function ratio β_A of the element X in phase A, which represents the equilibrium isotope fractionation factor between the phase A and an ideal gas of X atoms, can be expressed within the quasi-harmonic approximation as:

$$\beta_A = \frac{Q_h}{Q_l} = \prod_i^{3N} \frac{u_{ih}}{u_{il}} \frac{e^{-\frac{1}{2}u_{ih}}}{1-e^{-u_{ih}}} \frac{1-e^{-u_{il}}}{e^{-\frac{1}{2}u_{il}}} \qquad (1)$$

where *h* and *l* refer to the heavy and light isotopes respectively; *i* is a running index for the vibrational frequency, and *N* is the number of atoms in the unit cell. Q_h and Q_l represent the vibrational partition function for the heavy and light isotopes, respectively. Parameters u_{ih} and u_{il} are defined as:

$$u_{ih\ or\ il} = \hbar\omega_{ih\ or\ il}/k_B T \qquad (2)$$

Parameters $\hbar$ and k_B are the reduced Planck and Boltzmann constants, respectively; *T* is temperature in Kelvin, and $\omega_{ih\ or\ il}$ is the vibrational frequency of the i^{th} mode.

Notably, β in Eq. (1) is volume-dependent as phonon frequencies from the DFT+*U* calculations are a function of volume. In order to express β as a function of pressure (*P*) and temperature (*T*), we calculated the equation of state *V(P, T)* from the Helmholtz free energy, which can be written within the quasi-harmonic approximation as:

$$F(V,T) = U(V) + \frac{1}{2}\sum_{q,m}\hbar\omega_{q,m}(V) + k_B T \sum_{q,m} ln\,(1 - exp\,(-\frac{\hbar\omega_{q,m}(V)}{k_B T}) \qquad (3)$$

where *q* is a wave vector in the Brillouin zone and *m* is a running index of phonon mode. The first, second, and third terms in Eq. (3) correspond to the static, zero-point, and vibrational energy contributions, respectively. The calculated Helmholtz free energy versus volume was fitted by the third-order Birch–Murnaghan finite strain equation of state. Consequently, the pressure- and temperature-dependent β can be derived and the equilibrium isotope fractionation factor between two Phases A and B can be obtained in per mil (‰) as:

$$\Delta_{A-B} \approx 10^3 ln\alpha_{A-B} = 10^3 ln\beta_A - 10^3 ln\beta_B \qquad (4)$$

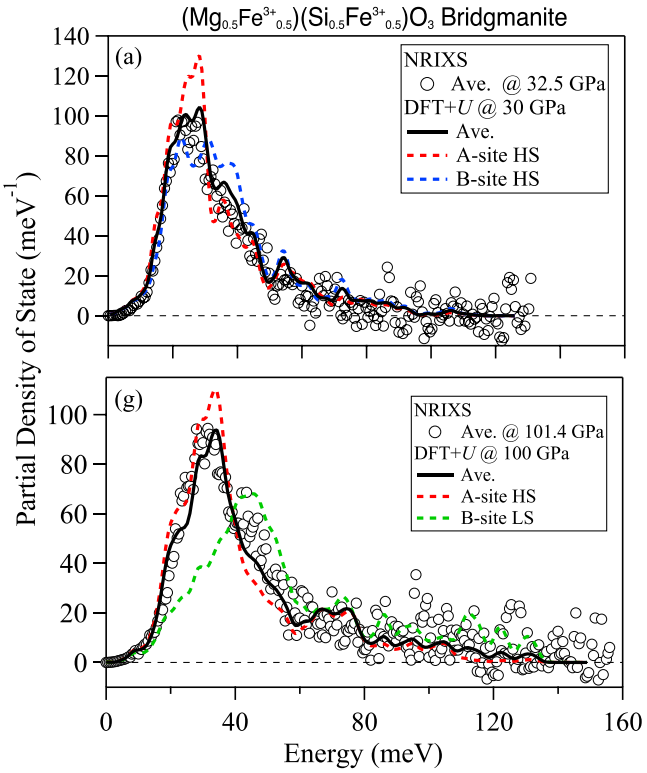

Figure 2. Representative partial phonon density of states (PDOS) of Fe^{3+} in $(Mg_{0.5}Fe^{3+}_{0.5})(Si_{0.5}Fe^{3+}_{0.5})O_3$ bridgmanite derived from both NRIXS measurements and DFT+*U* calculations. The open circles are the averaged PDOS of all Fe ions in the Bdg measured by NRIXS; (a): 32.5 GPa, (b): 101.4 GPa. The blue dotted, red dashed, and green dashed curves are the PDOS of A-site HS Fe^{3+}, B-site HS Fe^{3+} and B-site LS Fe^{3+} from DFT+*U* calculations, respectively. The black curves represent best-fit linear mixing model between DFT+*U* calculated PDOS of the A-site and B-site Fe^{3+}. The best-fit ratio of the weights is 50:50 for A-site and B-site HS Fe^{3+} PDOS in (a); the ratio changes to 70:30 for A-site HS and B-site LS Fe^{3+} PODS in (b).

3. Results

3.1 Partial phonon density of state of Fe in bridgmanite

For all pressures investigated, the calculated PDOS of Fe agree well with experimental PDOS (Fig. 2 and S1). Theoretical calculations provide the PDOS of the A-site and B-site Fe^{3+} individually, while the PDOS of Fe in $(Mg_{0.5}Fe^{3+}_{0.5})(Si_{0.5}Fe^{3+}_{0.5})O_3$ Bdg derived from NRIXS measurements is a sum of

contributions from both A-site and B-site Fe^{3+}. Comparisons between experimental observations of the PDOS, predictions for individual sites, and best-fit weighted average of calculated PDOS are shown for two representative pressures (Fig. 2). In theory, the ratio of A-site and B-site Fe^{3+} contributions to the final PDOS is the concentration ratio, 50:50. At ~30 GPa, the dominant peaks in the predicted PDOS of the A-site and B-site HS Fe^{3+} are located at ~17-31 meV and 17-43 meV, respectively (Fig. 2a). A 50-50 average of these calculated PDOS for A-site HS Fe^{3+} and B-site HS Fe^{3+} by DFT+*U* matches well with the experimental PDOS (Fig. 2a). This is in good agreement with the X-ray emission spectroscopy analysis that Bdg is 100% HS at this pressure (Liu et al., 2018). At ~100 GPa, DFT+*U* calculations indicate that the transition of B-site HS Fe^{3+} to LS state significantly change the PDOS: compared with the B-site HS Fe^{3+}, the predicted PDOS of the B-site LS Fe^{3+} is narrower and the dominant peaks are located at higher energies by ~11.7 meV (Fig. 2b). Accordingly, NRIXS observations demonstrate a shift of the major peak to higher energy, from ~25 meV at 30 GPa to ~30 meV at 100 GPa, and an increase in intensity at ~45 meV due to this B-site LS Fe^{3+} component. In order to match experimentally derived PDOS, the best weights of the calculated PDOS of A-site HS Fe^{3+} and B-site LS Fe^{3+} are 70:30 (Fig. 2b). This difference in weight ratio implies that the inelastic component of B-site LS Fe^{3+} from NRIXS measurements is significantly reduced across the spin transition. This is also consistent with the pressure dependence of the Lamb-Mössbauer factor (*f*) derived from NRIXS spectra (Fig. S2), which is directly controlled by the inelastic component ($S_{inelastic}$) in the NRIXS spectra (Dauphas et al., 2018):

$$f_{\mathrm{LM}} = 1 - \int_{E_{min}}^{E_{max}} S_{inelastic}\,(E)dE \qquad (5)$$

Across the spin transition of B-site Fe^{3+} in $(Mg_{0.5}Fe^{3+}_{0.5})(Si_{0.5}Fe^{3+}_{0.5})O_3$ Bdg, the linear slope of f_{LM} with respect to pressure increases from $6.7e^{-4}$ GPa^{-1} at 25-60 GPa to $1.6e^{-3}$ GPa^{-1} at ~60-70 GPa and changes to $3.7e^{-4}$ GPa^{-1} above ~70 GPa. Accounting for the change in the inelastic scattering profile of LS Fe^{3+}, NRIXS experiments and DFT+*U* calculation agree with complementary X-ray diffraction and X-ray emission spectroscopy observations about the conditions of the spin transition in Bdg.

3.2 Force constant of Fe and *β*-factors of $^{56}Fe/^{54}Fe$ for bridgmanite

From experimental and theoretical PDOS, the force constant of iron <*F*> and the β-factors of $^{56}Fe/^{54}Fe$ for $(Mg_{0.5}Fe^{3+}_{0.5})(Si_{0.5}Fe^{3+}_{0.5})O_3$ Bdg can be obtained within the harmonic approximation by following Eq. (6) and Eq. (7) (Dauphas et al., 2012):

$$< F >= \frac{M}{\hbar^2}\int_0^{+\infty} E^2\, g(E)dE \qquad (6)$$

$$10^3 ln\beta = 1000\left(\frac{1}{M^{54}\mathrm{Fe}} - \frac{1}{M^{56}\mathrm{Fe}}\right)\frac{\hbar^2}{8k^2T^2} < F > \qquad (7)$$

Here $g(E)$ is PDOS, M is the mass of a ^{54}Fe or ^{56}Fe nucleus, k is Boltzmann's constant and T is temperature in Kelvin. We find that <*F*> obtained from calculated PDOS are significantly larger than those calculated from experimental PDOS (Fig. 3), especially at pressures > 60 GPa, although the calculated PDOS match well with experimental PDOS (Fig. 2 and S1). To find out the factors that result in the <*F*> differences, we calculated the evolution of <*F*> by changing the upper limit of energy (x) for the integration by following Eq. (8):

$$< F >= \frac{M}{\hbar^2}\int_0^{x} E^2\, g(E)dE,\ (\text{x increases from 0 to } +\infty) \qquad (8)$$

As shown in Fig. 4, the integral values of <*F*> from calculated PDOS agree well with those from experimental PDOS until energy for the integration reaches a threshold, above which the predicted <*F*> still increases with x but the experimental one maintains a constant value (Fig. 4). This is mainly because the experimental PDOS intensity becomes indistinguishably close to zero due to the low signal noise ratio when energy is larger than 85 meV at 32.5 GPa and 110 meV at 101.4 GPa, while the predicted PDOS from DFT+U still have small non-zero values at these high-energy parts (Fig. 2). Amplified by the integral $E^2g(E)$, the small discrepancies in PDOS lead to significant differences in the final <*F*> by ~ 60 N/m at ~ 30 GPa and ~ 154 N/m at 100 GPa. Similarly, the predicted PDOS of A-site Fe^{3+} and Fe^{2+} in Bdg also agree well with experimental measurements (Yang et al., 2019), but the <*F*> from DFT+U are larger than experimental values, especially at high pressures (Fig. S3 and S4). In contrast, both of the calculated PDOS and <*F*> of LS Fe in Fp agree well with experimental results (Fig. S5). As a consequence, we use theoretical results of Bdg in this study and experimental data of HS and LS Fp from Yang et al. (2019) for further modelling and discussion.

Blanchard et al. (2015) found that compared to NRIXS, the DFT calculations

within GGA/GGA+U underestimate the <F> of iron in goethite. However, in their DFT calculations, the cell parameters of goethite were fixed to their experimental values and only atomic positions were relaxed. Because the GGA usually overestimates the volume, this incorrect strategy would put artificial stress on the structure and the true pressure from the GGA calculations should be higher than ambient pressure (Wang et al., 2017a; Wang et al., 2019b). This indicates that the iron <F> in Blanchard et al. (2015) was overestimated by their GGA/GGA+U calculations, and thus the <F> difference between NRIXS and DFT was underestimated. The discrepancy between NRIXS and GGA/GGA+U is mainly because the GGA underestimates the vibrational frequencies (Schauble, 2011), shifting the PDOS to lower values.

The changes of PDOS by different cation sites and spin states of Fe^{3+} result in variations in the corresponding $<F>$ and β-factors. For instance, as the PDOS of B-site HS Fe^{3+} concentrates at higher energy range compared with the corresponding A-site HS Fe^{3+} (Fig. 2 and S1), $<F>$ and β-factors are thus higher for HS Fe^{3+} in the B-site than that in the A-site (Fig. 3 and Fig. 5). Notably, across the spin transition of the B-site Fe^{3+} in $(Mg_{0.5}Fe^{3+}_{0.5})(Si_{0.5}Fe^{3+}_{0.5})O_3$ Bdg at ~ 60 GPa, the $<F>$ and β-factors of B-site Fe^{3+} increases by ~65%.

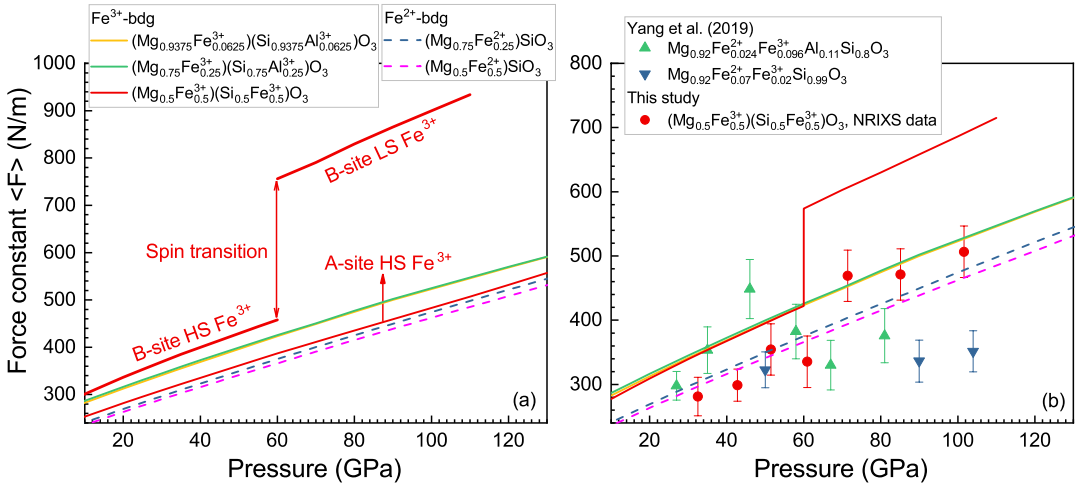

Figure 3. Force constant $<F>$ of iron in Bdg from DFT+U calculations. **(a)** $<F>$ of A-site Fe^{2+}, A-site Fe^{3+}, and B-site Fe^{3+} in Bdg. Compared with the $<F>$ of A-site Fe^{2+}, those of both A-site and B-site Fe^{3+} in Bdg are higher at the same pressure. Across the spin transition of the B-site Fe^{3+} in $(Mg_{0.5}Fe^{3+}_{0.5})(Si_{0.5}Fe^{3+}_{0.5})O_3$ Bdg at ~ 60 GPa, the $<F>$ of B-site Fe^{3+} increases by ~65%. **(b)** comparisons of in $<F>$ Bdg between theoretical and experimental results (Yang et al., 2019).

Although PDOS of Fe in Bdg from DFT+U agree well with experimental measurements (Fig. 2, Fig. S1, and Fig. S3-S4), the predicted <F> are significantly larger than those from experimental PDOS, especially at high pressures.

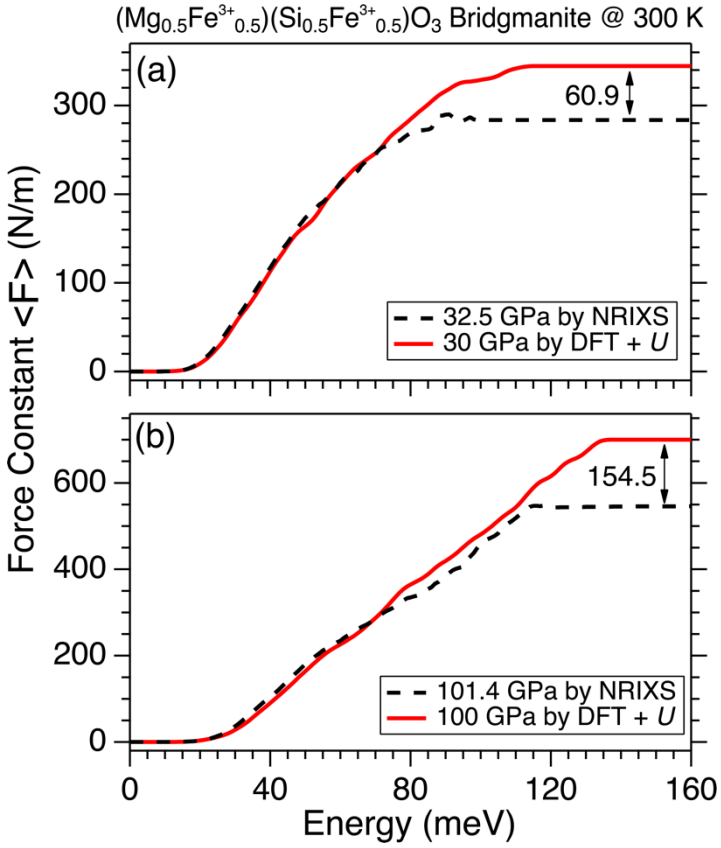

Figure 4. Evolution of <F> of Fe^{3+} in $(Mg_{0.5}Fe^{3+}_{0.5})(Si_{0.5}Fe^{3+}_{0.5})O_3$ Bdg with the upper limit of energy (x) for the integration $< F >= \frac{M}{\hbar^2}\int_0^x E^2\, g(E)dE$. The integral values of <F> from DFT+U calculations agree well with experimental results when x reaches a threshold, above which the predicted <F> still increases with x but the experimental one maintains a constant value.

On the other hand, the β-factors can be also calculated from Eq. (1) within the quasi-harmonic approximation (Urey equation). Following Bigeleisen and Mayer (1947) and Kowalski et al. (2013), when the β-factor is expressed by the Taylor expansions and the higher order terms are not taken into account, the Urey equation can be then approximated by Eq. (7). The validity criteria restricts the usage of Eq. (6) to frequencies $\nu\,[cm^{-1}] \leq 1.39\mathrm{T}\,[\mathrm{K}]$ (Bigeleisen and Mayer, 1947; Kowalski et al., 2013). Here we calculated the β-factors of Bdg with different chemical compositions

from their full phonon vibrational spectra using Eq. (1). Our calculated results show that the $10^3\ln\beta$ of Bdg decreases in the order of LS-$(Mg_{0.5}Fe^{3+}_{0.5})(Si_{0.5}Fe^{3+}_{0.5})O_3$ > HS-$(Mg_{0.5}Fe^{3+}_{0.5})(Si_{0.5}Fe^{3+}_{0.5})O_3$ > $(Mg_{0.9375}Fe^{3+}_{0.0625})(Si_{0.9375}Al^{3+}_{0.0625})O_3$ ≈ $(Mg_{0.75}Fe^{3+}_{0.25})(Si_{0.75}Al_{0.25})O_3$ > $(Mg_{0.75}Fe^{2+}_{0.25})SiO_3$ ≈ $(Mg_{0.5}Fe^{2+}_{0.5})SiO_3$ within calculated pressure range. At 60 GPa and 1000 K, it varies from 1.58‰ for LS-$(Mg_{0.5}Fe^{3+}_{0.5})(Si_{0.5}Fe^{3+}_{0.5})O_3$ to 0.98‰ for $(Mg_{0.5}Fe^{2+}_{0.5})SiO_3$ Bdg (Fig. 5a). Rustad and Yin (2009) also calculated the β factor of Fe^{2+}-bearing Bdg using molecular clusters and the $10^3\ln\beta$ of $^{56}Fe/^{54}Fe$ is ~1.44 ‰ at 120 GPa and 1000 K, similar to our predictions (1.42 ‰). However, it should be noted that the modelling of crystals using molecular clusters breaks the intrinsic periodic boundary of crystals.

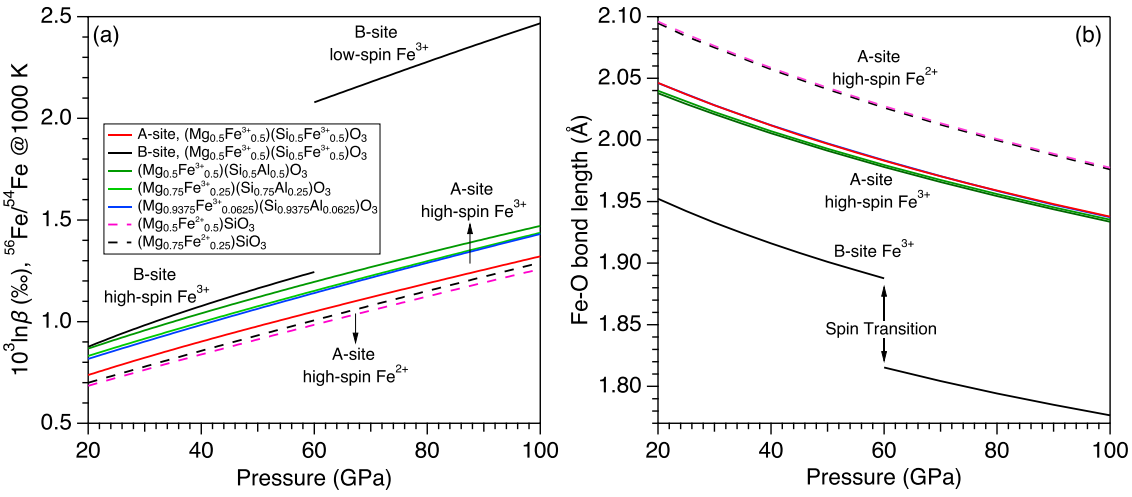

Figure 5. Comparisons between the $^{56}Fe/^{54}Fe$ β-factors and the Fe-O bond length of bdg at 30-100 GPa and 1000 K for different compositions in DFT+U calculations. (**a**) Compared with the β-factors of Fe^{2+} in the A-site of Bdg, those of both A-site and B-site Fe^{3+} in Bdg are higher at the same P-T condition. Across the spin transition of the B-site Fe^{3+} in $(Mg_{0.5}Fe^{3+}_{0.5})(Si_{0.5}Fe^{3+}_{0.5})O_3$ Bdg at ~ 60 GPa, the $^{56}Fe/^{54}Fe$ β-factor of B-site Fe^{3+} at 1000 K increases by 0.835‰. (**b**) The average Fe-O bond lengths in Bdg with different compositions at static conditions. Across the spin transition of B-site Fe^{3+} in $(Mg_{0.5}Fe^{3+}_{0.5})(Si_{0.5}Fe^{3+}_{0.5})O_3$ Bdg at ~ 60 GPa, the lengths of A-site and B-site Fe^{3+} decrease by 0.014 Å and 0. 0.072 Å, respectively. In contrast, the concentration effect on both A-site Fe^{2+}-O and A-site Fe^{3+}-O bond lengths in Bdg is negligible.

4. Discussion

4.1 Effects of site occupancy, spin transition, chemical composition, and valence state on β-factors of Bdg

The pressure dependences of β-factors of Bdg are controlled by multiple factors as shown in Fig. 2a. Here we show the β-factors anchored at 1000 K as a representative temperature to address these effects since the factors are almost linearly proportional to $1/T^2$ at different pressures (Fig. S6). In $(Mg_{0.5}Fe^{3+}_{0.5})(Si_{0.5}Fe^{3+}_{0.5})O_3$ Bdg, compared to the A-site HS Fe^{3+}, B-site HS Fe^{3+} has a higher β-factor and the difference between two sites is ~0.17‰ at 40 GPa and 1000 K (Fig. 5a). This is also consistent with the much shorter bond lengths, and correspondingly higher bond strength, of Fe^{3+}-O in the 6-coordinated B-site relative to the 8-coordinated A-site (Fig. 5b). B-site Fe^{3+} in Bdg is expected to undergo a HS to LS transition at middle-mantle depths (Catalli et al., 2010; Hsu et al., 2011; Mao et al., 2015; Shukla and Wentzcovitch, 2016; Fu et al., 2018b; Liu et al., 2018). The spin transition of the B-site Fe^{3+} in $(Mg_{0.5}Fe^{3+}_{0.5})(Si_{0.5}Fe^{3+}_{0.5})O_3$ Bdg occurs at ~ 50 GPa (Liu et al., 2018), which leads to shortening of the average B-site Fe^{3+}-O bonds by 0.072 Å, equal to 3.8% relative change (Fig. 5b). Such a change in the average Fe-O bond induces an increase of 0.83‰ in the β-factor of B-site Fe^{3+} at 1000 K and 0.21‰ at 2000 K (Fig. S6). However, the spin transition of the B-site Fe^{3+} does not significantly change the A-site Fe^{3+}-O bonds and the β-factor of A-site Fe^{3+}. Thus, the contrast between the β-factors of B-site and A-site Fe^{3+} is also strongly enhanced by the Fe spin transition in the B-site from 0.19‰ to 1.01‰ at 1000 K and 60 GPa (Fig. 5a).

The presence of Al in Bdg will weaken the effect of B-site Fe^{3+} spin transition on its β-factor by preventing Fe^{3+} from occupying the B-site. Depending on the bulk Al/Fe^{3+} molar ratio, Al^{3+} can either occupy the B-site only with Fe^{3+} filling in the A-site or it occupies both the B-site and the available A-site left by A-site Fe^{3+} (Lin et al., 2013; Liu et al., 2015). For Al/Fe^{3+} molar ratio equal to 1, all Fe^{3+} would occupy the A-site and all Al stays in the B-site. Here we calculated the β-factors of three Fe^{3+}- and Al-bearing Bdg with different $FeAlO_3$ concentration at 1000 K to illustrate the compositional dependence of both Fe^{3+}-O bond length and the β-factor of $^{56}Fe/^{54}Fe$ (Fig. 5a). Our results show that the incorporation of 6.25-50 mol% $FeAlO_3$ into Bdg only

changes the A-site Fe^{3+}-O bond length by 0-0.007 Å under lower-mantle pressures (Fig. 5b). As the Fe-O bond length controls the magnitude of the corresponding β-factor (Fig. S7), the effect of $FeAlO_3$ concentration on the β-factors of the A-site Fe^{3+} is insignificant. For example, the largest difference in the β-factor of Al^{3+}- and Fe^{3+}-bearing Bdg $(Mg_{0.9375}Fe^{3+}_{0.0625})(Si_{0.9375}Al^{3+}_{0.0625})O_3$, $(Mg_{0.75}Fe^{3+}_{0.25})(Si_{0.75}Al_{0.25})O_3$, and $(Mg_{0.5}Fe^{3+}_{0.5})(Si_{0.5}Al^{3+}_{0.5})O_3$ is smaller than 0.06‰ at 1000 K and all pressures (Fig. 5a). In contrast, the β-factor of A-site Fe^{3+} in $(Mg_{0.5}Fe^{3+}_{0.5})(Si_{0.5}Al^{3+}_{0.5})O_3$ Bdg is ~ 0.14‰ larger than that of A-site Fe^{3+} in $(Mg_{0.5}Fe^{3+}_{0.5})(Si_{0.5}Fe^{3+}_{0.5})O_3$ Bdg, consistent with relatively shorter Fe^{3+}-O bonds in the A site of $(Mg_{0.5}Fe^{3+}_{0.5})(Si_{0.5}Al^{3+}_{0.5})O_3$ Bdg (Fig. 5b). This reveals that the speciation of B-site ion (Fe^{3+} or Al^{3+}) also has a mild effect on the A-site Fe^{3+}-O bond strength and its β-factor. However, such an effect of Al on A-site Fe^{3+} β-factor is much weaker than the influence of spin transition and can be further diminished by mantle high temperatures, which results in only 0-0.01‰ difference in β-factor along the normal lower-mantle geotherm (Fig. 6). As long as some Fe^{3+} occupies the Bdg B-site, the change in β-factor due to the spin transition is independent of the identity of other ions on A- and B-site. Therefore, although Al^{3+} incorporation itself does not change the Bdg structure enough to impact isotopic fractionation, it prevents Fe^{3+} from occupying the B-site and thus reduces the significant impact of B-site Fe^{3+} spin transition on the β-factor of Bdg.

In addition to Fe^{3+}, the A site in Bdg is also large enough to accommodate Fe^{2+}, which maintains a HS state in Bdg throughout the lower mantle. The Fe^{2+}-bearing Bdg compositions in our DFT+U calculations, $(Mg_{0.5}Fe^{2+}_{0.5})SiO_3$ and $(Mg_{0.75}Fe^{2+}_{0.25})SiO_3$, have the smallest β-factors that are also insensitive to the Fe^{2+} content (Fig. 5a). This difference in β-factor between A-site Fe^{3+} and Fe^{2+} ranges from 0.04‰ to 0.15‰ at 1000 K (Fig. 5a) but will be diminished along an expected geotherm of the lower mantle (Fig. 6). In particular, the β-factor increases with pressure along the adiabat, because the increase due to compression outweighs the decrease from the $1/T^2$ dependence. The enrichment of light Fe isotopes in Fe^{2+}-bearing Bdg relative to other Fe^{3+}-bearing species is mainly caused by the longer Fe^{2+}-O bond lengths than those Fe^{3+}-O bonds (Fig. 5b and S7). Moreover, the valence state also partially contributes to the smaller β-factors of Fe^{2+}-bearing Bdg as revealed by the longer Fe-O bond length of HS A-site

Fe^{2+} than that of HS A-site Fe^{3+} (Fig. S7). In summary, the pressure- and temperature dependent β-factor of $^{56}Fe/^{54}Fe$ for Bdg is controlled by the Fe^{3+}/Fe^{2+}, Al/Fe^{3+}, and spin transition if there is some Fe^{3+} accommodated in B site.

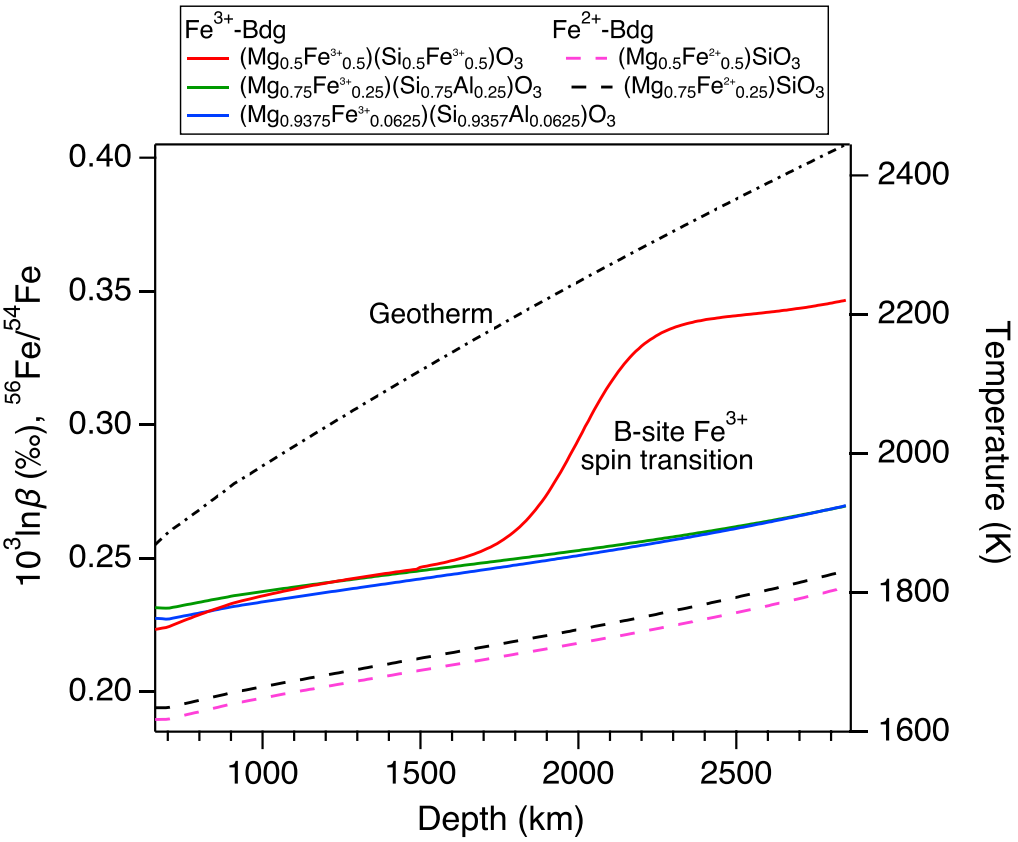

Figure 6. $^{56}Fe/^{54}Fe$ β-factors of various Bdg compositions computed by DFT+U along an adiabat representative of the average lower mantle. As the B-site Fe^{3+} undergoes high-spin to low-spin transition, the $^{56}Fe/^{54}Fe$ β-factor of $(Mg_{0.5}Fe^{3+}_{0.5})(Si_{0.5}Fe^{3+}_{0.5})O_3$ Bdg increases by ~0.09‰ across the spin transition of the B-site Fe^{3+}. The expected geotherm (dot dash line) was taken from Brown and McQueen (1986).

4.2 Fe isotopic fractionation in the deep mantle

4.2.1 Inter-mineral iron isotope fractionation

The $^{56}Fe/^{54}Fe$ β-factor of Bdg and Fp as a function of depth in likely bulk mantle compositions can be used to estimate fractionation of Fe isotopes in the deep Earth. The depth-dependence of Fe isotopic fractionation between Bdg and Fp in the lower mantle is modelled based on the following equations:

$$\Delta^{56}Fe_{Bdg\text{-}Fp} = \delta^{56}Fe_{Bdg} - \delta^{56}Fe_{Fp} \quad (9)$$

$$\delta^{56}Fe_{LM} = n_{Bdg} \times \delta^{56}Fe_{Bdg} + n_{Fp} \times \delta^{56}Fe_{Fp} \quad (10)$$

where $\delta^{56}Fe_{Bdg}$, $\delta^{56}Fe_{Fp}$, and $\delta^{56}Fe_{LM}$ are the Fe isotopic compositions of Bdg, Fp, and the bulk lower mantle, respectively. $\delta^{56}Fe_{LM}$ is set to 0 as the representative chondritic value (Craddock and Dauphas, 2011). n_{Bdg} and n_{Fp} are the Fe fractions in Bdg and Fp (Table S1), respectively, based on a pyrolitic lower mantle composition (Irifune et al., 2010). The pressure effect, including the pressure-induced spin transition, is taken into account on the evaluation of β-factors of Bdg and Fp.

Previous studies (Wang et al., 2015; Zhang et al., 2016; Wu, 2016) suggested that the lower mantle may be represented by a pyrolitic composition with ~ 8 wt% FeO and a Al/Fe ratio ~0.8 (McDonough and Sun, 1995). The lower-mantle $Fe^{3+}/\Sigma Fe$ ratio range was thought to be higher than 0.5 (Frost and McCammon, 2008), and the $Fe^{3+}/\Sigma Fe$ ratio of Bdg could be 0.5-1 for most part of the lower mantle (Wang et al., 2015). Because the site occupancy of Fe^{3+} is controlled by Al^{3+}/Fe^{3+} ratios (Frost et al., 2004; Lin et al., 2013; Liu et al., 2015; Liu et al., 2018), we consider three different endmembers for Bdg compositions: (1) Fe^{3+}- and Al^{3+}-free, Fe^{2+}-bearing; (2) Fe^{3+}- and Al^{3+}-bearing (3) Fe^{3+}-bearing but Al^{3+}-free (Fig. 7). These three endmembers demonstrate the range of possible compositional effects on Fe isotopic compositions of Bdg and Fp in the lower mantle:

1) For a simplified Fe^{3+}- and Al^{3+}-free, Fe^{2+}-bearing system, the major factor that impacts Fe-O bonds and Fe isotopic fractionation is the spin transition of Fe^{2+} in Fp at mid-lower-mantle depths. In this system, there is no significant iron fractionation between Bdg and Fp ($\Delta^{56}Fe_{Bdg\text{-}Fp}$ = 0-0.02‰) below 60 GPa. The spin transition occurs only in Fp at ~60-120 GPa, and increases the β-factor of Fp. This effect significantly decreases $\Delta^{56}Fe_{Bdg\text{-}Fp}$ from 0‰ at ~ 60 GPa to -0.17‰ at ~ 120 GPa (Fig. 7a). As a result, Fp would be enriched in ^{56}Fe with $\delta^{56}Fe_{Fp}$ up to 0-0.08‰ below mid-lower mantle and $\delta^{56}Fe_{Bdg}$ would be as low as -0.07‰ (Fig. 7b).
2) For a more realistic Fe^{3+}- and Al^{3+}-bearing system with the Fe^{3+}/Al ratio of < 1, our computational results suggest that the presence of Fe^{3+} in the Bdg A-site increases the β-factor of Bdg by 0.03-0.04‰ along an expected geotherm (Fig.

6). No significant difference across the spin transition of B-site Fe^{3+} in Bdg is expected in this composition relative to the Fe^{3+}- and Al^{3+}-free, but Fe^{2+}-bearing system. Therefore, $\Delta^{56}Fe_{Bdg\text{-}Fp}$ of the Fe^{3+}- and Al^{3+}-bearing system is ~0.03-0.04‰ higher than that of the simplified Fe^{3+}- and Al^{3+}-free, Fe^{2+}-bearing system (Fig. 7a). In this case, $\Delta^{56}Fe_{Bdg\text{-}Fp}$ decreases from +0.05‰ in the upper part of the lower mantle to -0.15‰ in the deeper part (Fig. 7b). This results in $\delta^{56}Fe_{Bdg}$ of +0.02‰ in the uppermost lower mantle but the number decreases to ~ -0.07‰ in the lowermost lower mantle (Fig. 7b).

3) In a Fe^{3+}- bearing but Al^{3+}-free system, the spin transitions of both Fe^{2+} in Fp and B-site Fe^{3+} in Bdg are expected to occur at the middle mantle depths and extend to the deeper part (Fig. 7a). Consequently, $\Delta^{56}Fe_{Bdg\text{-}Fp}$ in Fe^{3+}- bearing and Al^{3+}-free system is significantly higher than the other two systems beneath the middle mantle depths (Fig. 7a). The spin transition in B-site Fe^{3+} of Bdg results in $\delta^{56}Fe_{Bdg}$ as high as +0.04‰ in the middle mantle depth, which decreases to -0.03‰ in the lowermost lower mantle (Fig. 4b).

In a pyrolitic lower mantle, Fe^{3+} is generally not expected to occupy the B-site of Bdg as the Al/Fe^{3+} ratios of synthesized Bdg samples from pyrolitic starting materials are consistently higher than 1 (summarized in Shim et al., 2017). Harzburgite has a similar iron content but less Al_2O_3 content (~0.6%) compared to pyrolite (Irifune and Ringwood, 1987) and its $Fe^{3+}/\Sigma Fe$ ratio is usually < 5% (Canil and O'Nell, 1996; Woodland et al., 2006). As such, the Fe^{3+}/Al ratio in harzburgite is typically < 0.5 and no Fe^{3+} would occupy the B-site of Bdg when Bdg crystallizes from a harzburgitic composition. Therefore, the $\Delta^{56}Fe_{Bdg\text{-}Fp}$ in a pyrolitic or harzburgitic composition is similar to the results in scenarios (1) and (2). On the other hand, Fe^{3+}-rich materials (such as banded iron formation and goethite) could be carried to the lower mantle by subducted slabs, resulting in local chemical heterogeneous regions enriched in Fe^{3+}. Under such a scenario, Bdg may have much lower Al content and higher Fe^{3+} content, and therefore more Fe^{3+} could occupy both the A-site and B-site by the coupled substitution mechanism (Frost et al., 2004; Liu et al., 2015; Shim et al., 2017; Liu et al., 2018). Compared with Fe^{3+}- and Al^{3+}-bearing Bdg forming in a pyrolitic composition, the spin transition of the B-site Fe^{3+} in Bdg would increase $\Delta^{56}Fe_{Bdg\text{-}Fp}$ by as much as

0.08‰ (Fig. 7b), which slightly exceeds the highest precision measurements of $\delta^{56}Fe$ (~ 0.03‰, Sossi et al., 2015). Overall, Fe isotopic fractionation between Bdg and Fp is insignificant in most parts of the lower mantle, except the lowermost parts (Fig. 7). In the upper and middle part of the lower mantle, the stronger Fe-O bond strength in Fe^{3+}-enriched Bdg would only enrich Bdg in ^{56}Fe with $\delta^{56}Fe_{Bdg}$ as high as +0.02‰, with correspondingly indistinguishable $\Delta^{56}Fe_{Bdg\text{-}Fp}$ in these depths based on the highest precision of MC-ICP-MS measurements (~ 0.03‰, Sossi et al., 2015). In the lowermost lower mantle, the spin transition of Fe^{2+} in Fp would lead to the enrichment of heavy Fe in Fp with $\Delta^{56}Fe_{Bdg\text{-}Fp}$ as low as -0.15‰ in a pyrolitic composition. For the Fe^{3+}-rich but Al-poor system, the spin transition of B-site Fe^{3+} in Al-poor Bdg would diminish $\Delta^{56}Fe_{Bdg\text{-}Fp}$, making the Fe isotopic compositions of the coexisting oxidized Bdg and Fp indistinguishable (Fig. 7b). Therefore, the magnitude of $\Delta^{56}Fe_{Bdg\text{-}Fp}$ in a pyrolitic composition would probably exceed the technical resolution for Fe isotope measurements in the lowermost lower mantle, whereas no significant $\Delta^{56}Fe_{Bdg\text{-}Fp}$ would be found in the Fe^{3+}-rich but Al-poor system.

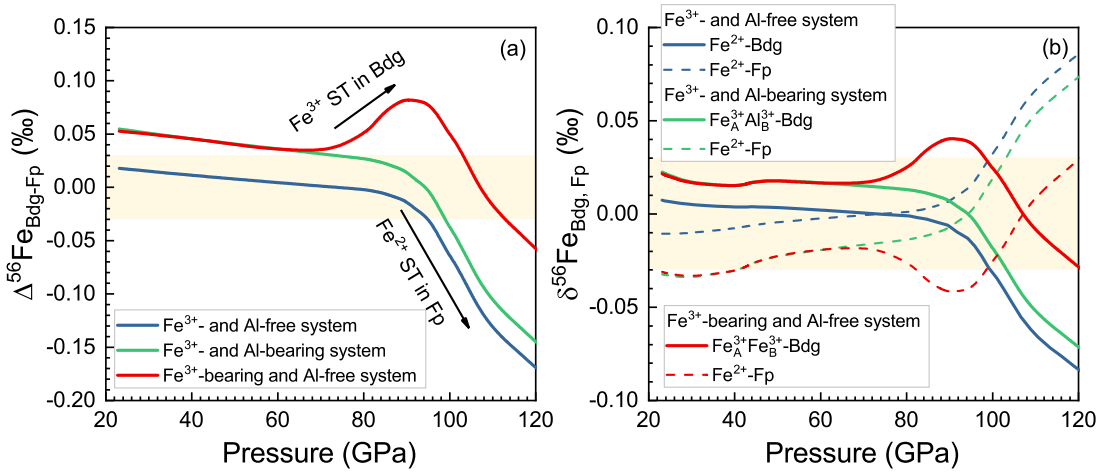

Figure 7. Equilibrium $^{56}Fe/^{54}Fe$ isotopic fractionation between coexisting Bdg and Fp (a) and the corresponding Fe isotopic compositions of these two phases (b) along an expected geotherm (Brown and McQueen, 1986). Solid and dash lines in (b) represent Fe isotopic compositions of Bdg and Fp, respectively. Three compositional assemblages are considered: Fe^{3+}-bearing but Al-free system (red curves); Fe^{3+}- but Al-bearing system (green curves) and Fe^{3+}- and Al-free system (blue curves). The light yellow areas represent the best resolution of MC-ICP-MS measurements (~ 0.03‰, Sossi et al., 2015). The spin transition (ST) of Fe^{2+} in Fp would occur

at the middle depth of the lower mantle, where only the B-site Fe^{3+} in Bdg would undergo a HS to LS transition at ~60 GPa.

4.2.2 Iron isotope fractionation during magma ocean crystallization

In addition to the possible Fe isotope fractionation between solid phases, how Fe isotopes would be fractionated between silicate melts and minerals during magma ocean crystallization (Boukaré et al., 2015) is also important for understanding the variability in iron isotopic composition in deep mantle (Yang et al., 2019). Based on the $<F>$ of solid phases and basaltic glass, Yang et al. (2019) investigated the evolution of Fe isotopic fractionation during terrestrial magma ocean crystallization and found no significant Fe fractionation between minerals and silicate melts. Here, following the model proposed in Yang et al. (2019), we also revaluated the Fe isotope fractionation between Bdg+Fp and silicate melts during magma ocean crystallization using the $<F>$ of Bdg from DFT+U calculations in this study. The <F> of solid phase was calculated from the <F> of Fp and Bdg using $<F>_{sum}=n_{Fp}*<F>_{Fp}+n_{Bdg}*<F>_{Bdg}$, where n_{Fp} and n_{Bdg} are the fractions of iron in Fp and Bdg in the solid phase, respectively, and $n_{Fp}+n_{Bdg}=1$. The $<F>$ of basaltic glass extrapolated to 130 GPa was used as an analogue to basaltic melts (Liu et al., 2017). The chemical compositions of solid aggregates and the residual melt were calculated after each 1 wt% increment of crystallization and can be found in Yang et al. (2019). Fractional crystallization and a mass-balance relationship were used in the model. For the i^{th} separation of solids, the isotopic composition of solids equilibrated with the residual melt can be calculated by $\delta^{56}Fe_{solids\text{-}i+1}=\delta^{56}Fe_{melts\text{-}i}+\Delta^{56}Fe_{solids\text{-}melts}$. Based on the isotopic mass balance, we have:

$$\delta^{56}Fe_{melts\text{-}i+1}=[\delta^{56}Fe_{melts\text{-}i}-(\delta^{56}Fe_{melts\text{-}i}+\Delta^{56}Fe_{solids\text{-}melts})*n_{solid}]/(1-n_{solids}) \quad (11)$$

$$\delta^{56}Fe_{solids\text{-}i+1}=-\delta^{56}Fe_{melts\text{-}i+1}*n_{melts}/(1-n_{melts}) \quad (12)$$

where n_{solids} is the fraction of iron taken up by solids at each step and n_{melts} is the fraction of total iron in the remaining melt. We note that the chemical composition of residual melt would be dominated by FeO (Fe/(Fe+Mg) > 60%) when the fraction of melt is lower than 10% with temperature decreasing to 4200 K (Figure 7 in Boukaré et al., 2015). At this stage, the $<F>$ of basaltic glass may not be used as an analogue to silicate melts due to the large difference in chemical compositions, and we stopped the

575 simulations.

576 Our results show that silicate melts are isotopically lighter than Bdg+Fp but the
577 $\Delta^{56}Fe_{solids\text{-}melts}$ are smaller than +0.03‰ for Fe^{2+}-bearing and Fe^{3+}-free systems and
578 Fe^{3+}- and Al^{3+}-bearing system. As Fe^{3+} is generally not expected to occupy the Bdg B-
579 site in a pyrolitic lower mantle with the Al/Fe^{3+} ratios of higher than 1, it can be
580 concluded that no significant Fe isotope fractionation between Bdg+Fp and silicate melt
581 has been produced during the crystallization process. For the Fe^{3+}-bearing but Al-poor
582 system, $\Delta^{56}Fe_{solids\text{-}melts}$ could be up +0.06‰, if we also used the $<F>$ of basaltic melts
583 as an analogue to Fe^{3+}-rich melts. However, Fe^{3+}-rich melts should be expected to be
584 enriched in heavy Fe isotopes relative to the Fe^{2+}-rich one (Dauphas et al., 2014),
585 because the <F> of Fe^{3+}-bearing silicate glass is ~150 N/m larger than that of Fe^{2+}-
586 bearing silicate glass (Dauphas et al., 2014). As a result, the $<F>$ of Fe^{3+}-rich melts
587 were underestimated in this case and the $\Delta^{56}Fe_{solids\text{-}melts}$ (up +0.06‰) could have been
588 overestimated by 0.025‰, if the $<F>$ difference between Fe^{3+}-rich and Fe^{2+}-rich melts
589 at 130 GPa is modeled by the value for silicate glasses at ambient pressure (Dauphas et
590 al., 2014). Although the $<F>$ of Fe^{3+}-rich melts at 130 GPa are still unknown, the
591 crystallization process of Fe^{3+}-rich melts in some local regions also cannot produce
592 resolvable Fe isotope fractionation between solids and melts. Therefore, we suggest that
593 crystallization of the magma ocean is unlikely to have resulted in significant iron
594 isotopic fractionation in deep mantle.
595

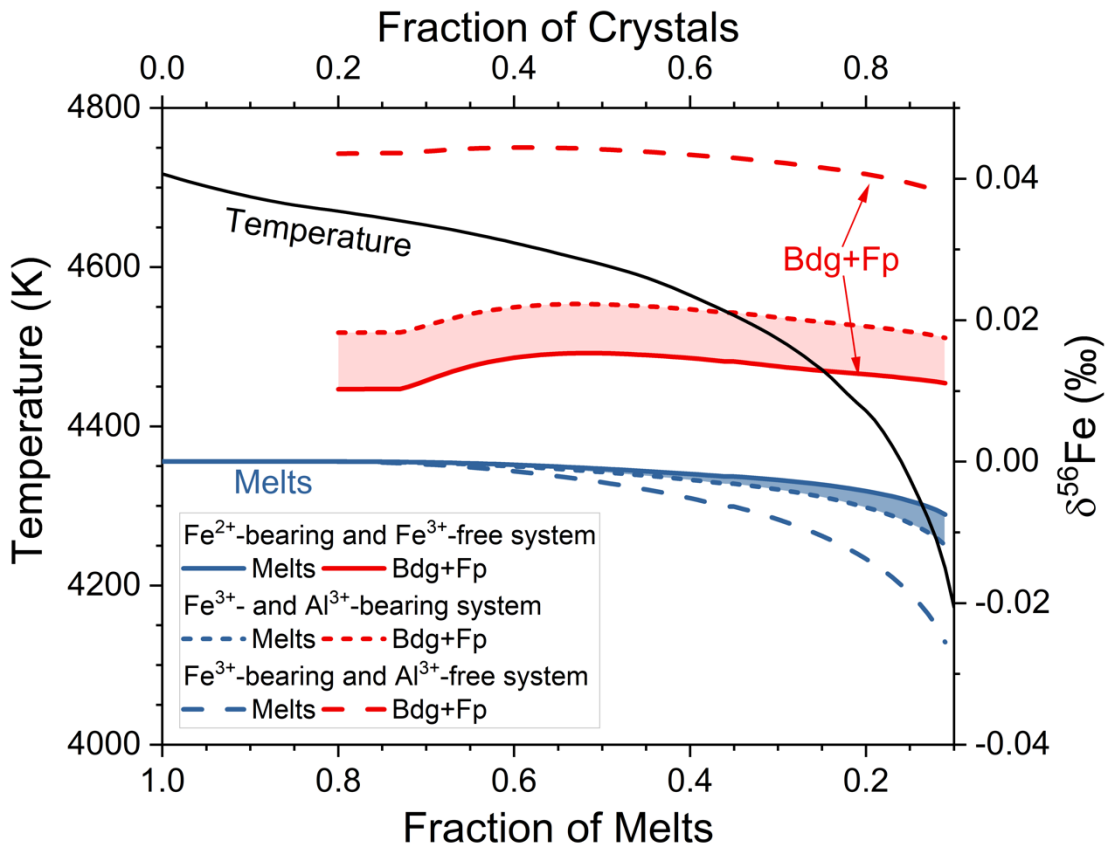

596

597 **Figure 8.** Equilibrium Fe isotope fractionation between solids and melts during magma ocean
598 crystallization at 130 GPa. The modelling details were described in details in Yang et al. (2019).
599 Similarly, the initial δ^{56}Fe of magma ocean is set as 0‰ and the solid crystallization sequence
600 was obtained from Boukaré et al. (2015). Red and blue lines represent δ^{56}Fe of solids (Bdg+Fp)
601 and melts, respectively. Solid, short dash, and dash lines refer to Fe^{2+}-bearing and Fe^{3+}-free,
602 Fe^{3+}- and Al^{3+}-bearing, and Fe^{3+}-bearing and Al^{3+}-free systems, respectively. The $<F>$ of solids
603 and melts at 130 GPa are used for modelling. Data sources: Bdg, DFT+*U* calculations in this
604 study; Fp, extrapolated to 130 GPa, Yang et al. (2019); melts, imitated by basaltic glass,
605 extrapolated to 130 GPa (Liu et al., 2017). The case for a pyrolitic composition, in which both
606 Fe^{2+} and Fe^{3+} could be present but Fe^{3+} is not expected to occupy the Bdg B-site, can be
607 represented by shade areas enclosed by solid and short dash lines.

608

609 **4.3 Fe isotope fractionation between core and mantle**

610 Mid-ocean ridge basalts (MORB) in the Earth were found to be enriched in heavy
611 Fe isotopes ($^{56}Fe/^{54}Fe$) by ~+0.1‰ relative to the chondrites (Teng et al., 2013), while
612 basalts from Mars and Vesta have Fe isotope compositions similar to the chondrites

(Sossi et al., 2016; Elardo and Shahar, 2017). The elevated $^{56}Fe/^{54}Fe$ ratio in MORB was thought to be caused by mantle partial melting (Teng et al., 2008; Dauphas et al., 2014), but this process can only induce an iron isotopic shift of +0.023‰ (Dauphas et al., 2014). Some other interpretations, including loss of light Fe isotopes during vaporization and condensation (Poitrasson et al., 2004; Poitrasson, 2007), core formation (Polyakov, 2009; Elardo and Shahar, 2017), have been proposed to enrich Earth's mantle in heavy Fe isotopes. Some studies suggested that the Fe isotope composition of mantle peridotites is close to that of chondrites (Poitrasson, 2007; Craddock et al., 2013), while it has been argued that mantle peridotites may be slightly heavier (~+0.05 ‰) than chondrites (Poitrasson et al., 2013; Sossi et al., 2016). It is not well-known whether the Fe isotope composition of the primitive mantle has been modified by core formation.

In order to check the effect of core formation on the Fe isotope composition of bulk silicate Earth, previous studies have widely investigated the $<F>$ of metallic alloys (Chen et al., 2014; Shahar et al., 2016; Liu et al., 2017; Chen et al., 2018) and basaltic glass (Liu et al., 2017), which were used as analogues to metallic and silicate melts, respectively. In addition, Fe^{2+}-bearing Bdg was also used as the analogue to silicate melt (Shahar et al., 2016). Here we also assume that the $<F>$ of silicate melts could be represented by those of Bdg, as we find that Fe^{2+}-bearing and Fe^{3+}-free Bdg has similar $<F>$ to the Fe^{2+}-bearing basaltic glass at 40-60 GPa (Fig. 9). Our results show that Bdg has relatively larger $<F>$ than metallic alloys and the $<F>$ difference between Bdg and metallic alloys depends on their chemical compositions (Fig. 9). Using the high-temperature approximation, we conclude that the equilibrium Fe isotope fractionation between silicate and metallic melts is ~0-0.04‰ under core-formation conditions for the Earth (~40-60 GPa and 3500 K) (Li and Agee, 1996; Siebert et al., 2012; Fischer et al., 2015). This implies that core formation can only shift the Fe isotope composition of Earth's mantle by 0-0.04‰, which is not sufficient to account for the enrichment of heavy Fe isotopes in MORB with the consideration of partial melting.

In contrast, heavy Fe isotopes might be enriched in the lowermost lower mantle with respect to the adjacent liquid outer core, as low-spin Fe species likely to be present in phases at the base of the mantle are expected to have high β-factors and

corresponding force constants <*F*> (Fig. 9). At *P-T* conditions near the CMB, Fe^{2+} is expected to adopt LS state in both solid and liquid FeO-MgO system (Mao et al., 2011; Fu et al., 2018a; Yang et al., 2019); while Fe^{3+} in the octahedral site of both Bdg and Ppv is expected to adopt LS state (Catalli et al., 2010; Yu et al., 2012; Liu et al., 2018). At a representative *P-T* condition near the CMB (130 GPa and 3000 K), the calculated $\Delta^{56}Fe_{Bdg\text{-}core}$ from the corresponding <*F*> with LS Fe^{3+} in the B-site of Bdg could range from +0.09‰ to +0.12‰ for various outer core compositions, such as Si, S and C (Fig. 9), if there is a chemical exchange and equilibration of solid mantle with outer core. $(Fe^{2+}, Mg)SiO_3$–Ppv was found to be enriched in heavy iron isotopes relative to metallic iron with $\Delta^{56}Fe_{Ppv\text{-}core}$ of ~0.1‰ at the CMB (Polyakov, 2009), and Fe^{3+}-bearing Ppv should be more enriched in heavy iron isotopes. Meanwhile, $\Delta^{56}Fe_{Fp\text{-}core}$ ranges from +0.17‰ to +0.20‰ for CMB regions with high concentrations of LS FeO, such as some ultra-low velocity zones (Wicks et al., 2010; Fu et al., 2018a). These fractionation factors suggest that Fe isotopes might be redistributed during the mantle-core interaction and some local regions above the CMB could be enriched in heavy Fe isotopes. However, whether such a Fe isotopic signature could be produced and preserved or not also depends on the interaction pattern and the geodynamic mantle convention (Lesher et al., 2020).

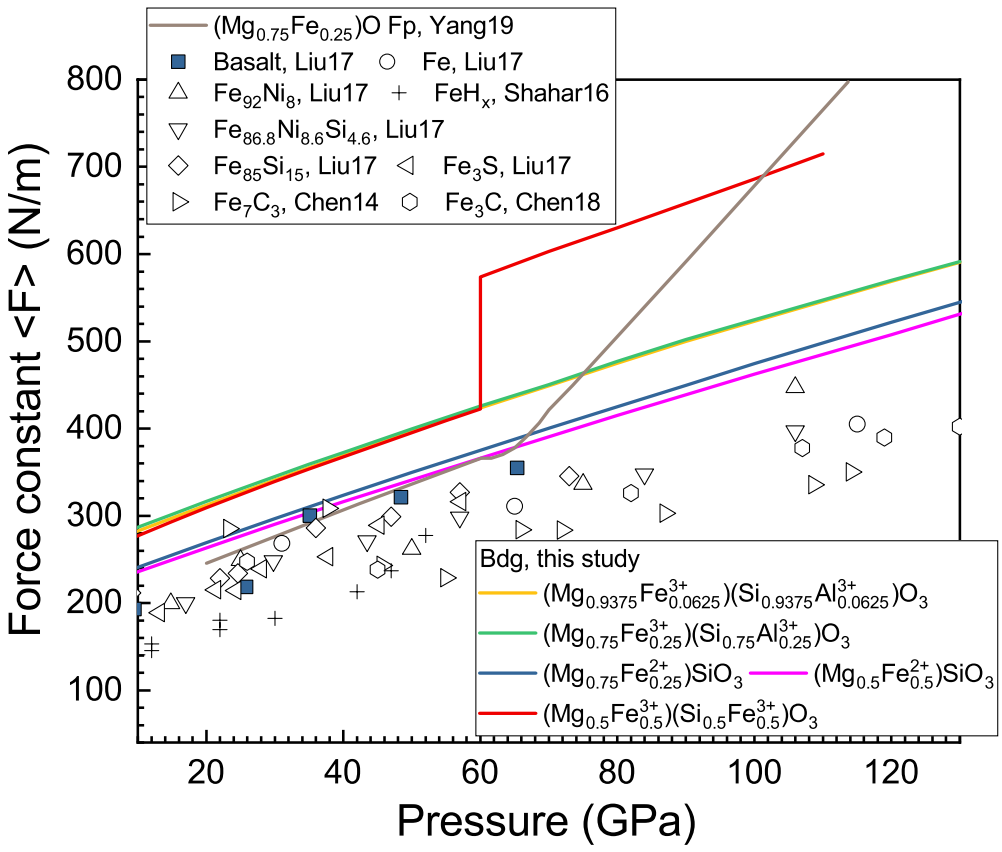

Figure 9. Comparison of force constants <*F*> of Bdg computed in this work with previous studies of Fp and Fe/Fe alloys. At a given *P*-*T* condition, Fe equilibrium isotopic fractionation factor can be obtained by following $\Delta^{56}Fe_{A\text{-}B}=2940\ (<F>_A-<F>_B)/T^2$. Experimental data sources: Bdg, this study; $(Mg_{0.75}Fe_{0.25})O$ Fp, Yang et al. (2019); Basaltic glass ($Na_{0.036}Ca_{0.220}Mg_{0.493}Fe_{0.115}Al_{0.307}Ti_{0.012}K_{0.002}Si_{0.834}O_3$), Fe, $Fe_{86.8}Ni_{8.6}Si_{4.6}$, $Fe_{85}Si_{15}$, Fe_3S: Liu et al. (2017); Fe_7C_3: Chen et al. (2014); Fe_3C: Chen et al. (2018); FeHx: Shahar et al. (2016).

5. Conclusion

We have investigated the effects of site occupancies, chemical composition, spin transition, and valence state on the reduced Fe partition function ratio (β-factor) of (Mg, Fe^{2+}, Fe^{3+}, Al^{3+})(Fe^{3+}, Al^{3+}, Si)O_3 Bdg under lower-mantle pressure-temperature conditions by performing first-principles calculations and synergistic nuclear resonant inelastic X-ray scattering measurements. The computational partial phonon density of states of Fe^{3+} in $(Mg_{0.5}Fe^{3+}_{0.5})(Si_{0.5}Fe^{3+}_{0.5})O_3$ bridgmanite agree well with experimental measurements at high pressures. Our results reveal that Fe^{2+}-bearing Bdg has the smallest β-factor relative to other Fe^{3+}-bearing species. Site occupancies for Fe^{3+} can

have a significant effect on the β-factor of Bdg. Compared to the A-site HS Fe^{3+}, the B-site HS Fe^{3+} has a higher β-factor by ~0.17‰ at 40 GPa and 1000 K. The spin transition of B-site Fe^{3+} in Bdg influences its β-factor more significantly than variations in valence state and chemical composition, with an increase of ~ +0.83‰ across the spin transition at 1000 K. This change would be diminished to +0.09‰ along an expected geotherm of the lower mantle. The variation of β-factors is mainly controlled by the Fe-O bond lengths, and the shorter bond lengths correspond to higher bond strength and β-factors. In addition, although the incorporation of Al^{3+} into the Bdg B-site results in a mild effect on the β-factor of A-site Fe^{3+} when compared to $(Mg_{0.5}Fe^{3+}_{0.5})(Si_{0.5}Fe^{3+}_{0.5})O_3$ Bdg, the presence of Al in Earth's lower mantle would decrease the impact of B-site Fe^{3+} spin transition on the β-factor of Bdg by preventing Fe^{3+} from occupying the B-site. Combined with previous data, our models demonstrate that Fe isotopic fractionation between Fp and Bdg in most parts of the lower mantle would not be significant, except the lowermost parts. The crystallization of the magma ocean is also unlikely to have resulted in significant iron isotopic fractionation in any deep-mantle reservoir. In contrast, under the conditions of the core-mantle boundary, low-spin Fe-bearing mantle minerals could concentrate heavy Fe isotopes by up to +0.20‰ through core-mantle interaction.

Acknowledgements

W.Z. Wang and Z.Q. Wu acknowledge the Strategic Priority Research Program of the Chinese Academy of Sciences (XDB18000000), the Natural Science Foundation of China (41721002, 41925017). J.F.L. acknowledges support from the Geophysics Program of the National Science Foundation (EAR-1502594). S.M.D. also acknowledges support from NSF CSEDI (EAR-1664332). NRIXS experiments used resources of the Advanced Photon Source, a U.S. Department of Energy (DOE) Office of Science User Facility operated for the DOE Office of Science by Argonne National Laboratory under Contract No. DE-AC02-06CH11357. We are grateful to the constructive comments from Paolo Sossi and the other two anonymous reviewers and editorial handling by Mike Toplis and Jeffrey G. Catalano.

Research Data

Relevant data is provided in Electronic Supplementary materials.

References

Akahama Y. and Kawamura H. (2010) Pressure calibration of diamond anvil Raman gauge to 410 GPa. *J. Phys. Conf. Ser.* **215**, 012195. Available at: http://stacks.iop.org/1742-6596/215/i=1/a=012195?key=crossref.e13853a2cfe73464df62698f42525ac4.

Andrault D., Muñoz M., Pesce G., Cerantola V., Chumakov A., Kantor I., Pascarelli S., Rüffer R. and Hennet L. (2018) Large oxygen excess in the primitive mantle could be the source of the Great Oxygenation Event. *Geochemical Perspect. Lett.*, 5–10. Available at: http://www.geochemicalperspectivesletters.org/article1801.

Anisimov V. I., Zaanen J. and Andersen O. K. (1991) Band theory and Mott insulators: Hubbard U instead of Stoner I. *Phys. Rev. B* **44**, 943–954.

Armstrong K., Frost D. J., McCammon C. A., Rubie D. C. and Boffa Ballaran T. (2019) Deep magma ocean formation set the oxidation state of Earth's mantle. *Science (80-.).* **365**, 903–906.

Bigeleisen J. and Mayer M. G. (1947) Calculation of Equilibrium Constants for Isotopic Exchange Reactions. *J. Chem. Phys.* **15**, 261. Available at: http://scitation.aip.org/content/aip/journal/jcp/15/5/10.1063/1.1746492.

Blanchard M., Dauphas N., Hu M. Y., Roskosz M., Alp E. E., Golden D. C., Sio C. K., Tissot F. L. H., Zhao J., Gao L., Morris R. V., Fornace M., Floris A., Lazzeri M. and Balan E. (2015) Reduced partition function ratios of iron and oxygen in goethite. *Geochim. Cosmochim. Acta* **151**, 19–33. Available at: https://linkinghub.elsevier.com/retrieve/pii/S0016703714007157.

Boukaré C.-E., Ricard Y. and Fiquet G. (2015) Thermodynamics of the MgO-FeO-SiO 2 system up to 140 GPa: Application to the crystallization of Earth's magma ocean. *J. Geophys. Res. Solid Earth* **120**, 6085–6101. Available at: http://doi.wiley.com/10.1002/2015JB011929.

Brown J. M. and McQueen R. G. (1986) Phase transitions, Grüneisen parameter, and elasticity for shocked iron between 77 GPa and 400 GPa. *J. Geophys. Res. Solid Earth* **91**, 7485–7494. Available at: http://doi.wiley.com/10.1029/JB091iB07p07485.

CANIL D. and O'NEILL H. S. C. (1996) Distribution of Ferric Iron in some Upper-Mantle Assemblages. *J. Petrol.* **37**, 609–635. Available at: https://academic.oup.com/petrology/article-lookup/doi/10.1093/petrology/37.3.609.

Catalli K., Shim S. H., Prakapenka V. B., Zhao J. and Sturhahn W. (2010) X-ray diffraction and Mössbauer spectroscopy of Fe3+- bearing Mg-silicate post-perovskite at 128-138 GPa. *Am. Mineral.* **95**, 418–421.

Catalli Krystle, Shim S. H., Prakapenka V. B., Zhao J., Sturhahn W., Chow P., Xiao Y., Liu H., Cynn H. and Evans W. J. (2010) Spin state of ferric iron in MgSiO3 perovskite and its effect on elastic properties. *Earth Planet. Sci. Lett.* **289**, 68–75. Available at: http://dx.doi.org/10.1016/j.epsl.2009.10.029.

755 Chen B., Lai X., Li J., Liu J., Zhao J., Bi W., Ercan Alp E., Hu M. Y. and Xiao Y.
756 (2018) Experimental constraints on the sound velocities of cementite Fe3C to
757 core pressures. *Earth Planet. Sci. Lett.* **494**, 164–171. Available at:
758 https://doi.org/10.1016/j.epsl.2018.05.002.
759 Chen B., Li Z., Zhang D., Liu J., Hu M. Y., Zhao J., Bi W., Alp E. E., Xiao Y., Chow
760 P. and Li J. (2014) Hidden carbon in Earth's inner core revealed by shear
761 softening in dense Fe 7 C 3. *Proc. Natl. Acad. Sci.* **111**, 17755–17758. Available
762 at: http://www.pnas.org/lookup/doi/10.1073/pnas.1411154111.
763 Cococcioni M. and de Gironcoli S. (2005) Linear response approach to the calculation
764 of the effective interaction parameters in the LDA+U method. *Phys. Rev. B* **71**,
765 035105. Available at:
766 http://link.aps.org/doi/10.1103/PhysRevB.71.035105%5Cnhttp://arxiv.org/abs/co
767 nd-mat/0405160.
768 Craddock P. R. and Dauphas N. (2011) Iron Isotopic Compositions of Geological
769 Reference Materials and Chondrites. *Geostand. Geoanalytical Res.* **35**, 101–123.
770 Available at: http://doi.wiley.com/10.1111/j.1751-908X.2010.00085.x.
771 Craddock P. R., Warren J. M. and Dauphas N. (2013) Abyssal peridotites reveal the
772 near-chondritic Fe isotopic composition of the Earth. *Earth Planet. Sci. Lett.* **365**,
773 63–76. Available at: http://dx.doi.org/10.1016/j.epsl.2013.01.011.
774 Dauphas N., Hu M. Y., Baker E. M., Hu J., Tissot F. L. H., Alp E. E., Roskosz M.,
775 Zhao J., Bi W., Liu J., Lin J.-F., Nie N. X. and Heard A. (2018) SciPhon: a data
776 analysis software for nuclear resonant inelastic X-ray scattering with applications
777 to Fe, Kr, Sn, Eu and Dy. *J. Synchrotron Radiat.* **25**, 1581–1599.
778 Dauphas N., Roskosz M., Alp E. E., Golden D. C., Sio C. K., Tissot F. L. H., Hu M.
779 Y., Zhao J., Gao L. and Morris R. V. (2012) A general moment NRIXS approach
780 to the determination of equilibrium Fe isotopic fractionation factors: Application
781 to goethite and jarosite. *Geochim. Cosmochim. Acta* **94**, 254–275. Available at:
782 http://linkinghub.elsevier.com/retrieve/pii/S0016703712003663.
783 Dauphas N., Roskosz M., Alp E. E., Neuville D. R., Hu M. Y., Sio C. K., Tissot F. L.
784 H., Zhao J., Tissandier L., Médard E. and Cordier C. (2014) Magma redox and
785 structural controls on iron isotope variations in Earth's mantle and crust. *Earth*
786 *Planet. Sci. Lett.* **398**, 127–140.
787 Dorfman S. M., Potapkin V., Lv M., Greenberg E., Kupenko I., Chumakov A. I., Bi
788 W., Alp E. E., Liu J., Magrez A., Dutton S. E., Cava R. J., McCammon C. A. and
789 Gillet P. (2020) Effects of composition and pressure on electronic states of iron
790 in bridgmanite. *Am. Mineral.* **105**, 1030–1039. Available at:
791 https://pubs.geoscienceworld.org/msa/ammin/article/105/7/1030/587519/Effects-
792 of-composition-and-pressure-on-electronic.
793 Elardo S. M. and Shahar A. (2017) Non-chondritic iron isotope ratios in planetary
794 mantles as a result of core formation. *Nat. Geosci.* **10**, 317–321.
795 Feng C., Qin T., Huang S., Wu Z. and Huang F. (2014) First-principles investigations
796 of equilibrium calcium isotope fractionation between clinopyroxene and Ca-

doped orthopyroxene. *Geochim. Cosmochim. Acta* **143**, 132–142. Available at: http://dx.doi.org/10.1016/j.gca.2014.06.002.

Fischer R. A., Nakajima Y., Campbell A. J., Frost D. J., Harries D., Langenhorst F., Miyajima N., Pollok K. and Rubie D. C. (2015) High pressure metal–silicate partitioning of Ni, Co, V, Cr, Si, and O. *Geochim. Cosmochim. Acta* **167**, 177–194. Available at: https://linkinghub.elsevier.com/retrieve/pii/S0016703715004093.

Frost D. J., Liebske C., Langenhorst F., McCammon C. a, Tronnes R. G. and Rubie D. C. (2004) Experimental evidence for the existence of iron-rich metal in the Earth' s lower mantle. *Nature* **428**, 409–412.

Frost D. J. and McCammon C. A. (2008) The Redox State of Earth's Mantle. *Annu. Rev. Earth Planet. Sci.* **36**, 389–420. Available at: http://www.annualreviews.org/doi/10.1146/annurev.earth.36.031207.124322.

Fu S., Yang J., Zhang Y., Liu J., Greenberg E., Prakapenka V. B., Okuchi T. and Lin J. F. (2018a) Melting behavior of the lower-mantle ferropericlase across the spin crossover: Implication for the ultra-low velocity zones at the lowermost mantle. *Earth Planet. Sci. Lett.* **503**, 1–9. Available at: https://doi.org/10.1016/j.epsl.2018.09.014.

Fu S., Yang J., Zhang Y., Okuchi T., McCammon C., Kim H. I., Lee S. K. and Lin J. F. (2018b) Abnormal Elasticity of Fe-Bearing Bridgmanite in the Earth's Lower Mantle. *Geophys. Res. Lett.* **45**, 4725–4732.

Giannozzi P., Baroni S., Bonini N., Calandra M., Car R., Cavazzoni C., Ceresoli D., Chiarotti G. L., Cococcioni M., Dabo I., Dal Corso A., de Gironcoli S., Fabris S., Fratesi G., Gebauer R., Gerstmann U., Gougoussis C., Kokalj A., Lazzeri M., Martin-Samos L., Marzari N., Mauri F., Mazzarello R., Paolini S., Pasquarello A., Paulatto L., Sbraccia C., Scandolo S., Sclauzero G., Seitsonen A. P., Smogunov A., Umari P. and Wentzcovitch R. M. (2009) QUANTUM ESPRESSO: a modular and open-source software project for quantum simulations of materials. *J. Phys. Condens. Matter* **21**, 395502. Available at: http://stacks.iop.org/0953-8984/21/i=39/a=395502?key=crossref.c21336c286fa6d3db893262ae3f6e151.

Hsu H., Blaha P., Cococcioni M. and Wentzcovitch R. M. (2011) Spin-State Crossover and Hyperfine Interactions of Ferric Iron in MgSiO3 Perovskite. *Phys. Rev. Lett.* **106**, 118501. Available at: https://link.aps.org/doi/10.1103/PhysRevLett.106.118501.

Hsu H., Umemoto K., Blaha P. and Wentzcovitch R. M. (2010) Spin states and hyperfine interactions of iron in (Mg,Fe)SiO3 perovskite under pressure. *Earth Planet. Sci. Lett.* **294**, 19–26. Available at: https://linkinghub.elsevier.com/retrieve/pii/S0012821X10001330.

Huang F., Chen L., Wu Z. and Wang W. (2013) First-principles calculations of equilibrium Mg isotope fractionations between garnet, clinopyroxene, orthopyroxene, and olivine: Implications for Mg isotope thermometry. *Earth*

Planet. Sci. Lett. **367**, 61–70. Available at: http://dx.doi.org/10.1016/j.epsl.2013.02.025.

Huang F., Wu Z., Huang S. and Wu F. (2014) First-principles calculations of equilibrium silicon isotope fractionation among mantle minerals. *Geochim. Cosmochim. Acta* **140**, 509–520. Available at: http://dx.doi.org/10.1016/j.gca.2014.05.035.

Irifune T. and Ringwood A. E. (1987) Phase transformations in a harzburgite composition to 26 GPa: implications for dynamical behaviour of the subducting slab. *Earth Planet. Sci. Lett.* **86**, 365–376. Available at: https://linkinghub.elsevier.com/retrieve/pii/0012821X87902330.

Irifune T., Shinmei T., McCammon C. A., Miyajima N., Rubie D. C. and Frost D. J. (2010) Iron Partitioning and Density Changes of Pyrolite in Earth's Lower Mantle. *Science (80-.).* **327**, 193–195. Available at: http://www.sciencemag.org/lookup/doi/10.1126/science.1181443.

Kowalski P. M., Wunder B. and Jahn S. (2013) Ab initio prediction of equilibrium boron isotope fractionation between minerals and aqueous fluids at high P and T. *Geochim. Cosmochim. Acta* **101**, 285–301. Available at: http://dx.doi.org/10.1016/j.gca.2012.10.007.

Lesher C. E., Dannberg J., Barfod G. H., Bennett N. R., Glessner J. J. G., Lacks D. J. and Brenan J. M. (2020) Iron isotope fractionation at the core–mantle boundary by thermodiffusion. *Nat. Geosci.* **13**, 382–386. Available at: http://dx.doi.org/10.1038/s41561-020-0560-y.

Li J. and Agee C. B. (1996) Geochemistry of mantle–core differentiation at high pressure. *Nature* **381**, 686–689. Available at: http://www.nature.com/articles/381686a0.

Li J., Sturhahn W., Jackson J. M., Struzhkin V. V., Lin J. F., Zhao J., Mao H. K. and Shen G. (2006) Pressure effect on the electronic structure of iron in (Mg,Fe)(Si,Al)O3 perovskite: a combined synchrotron Mössbauer and X-ray emission spectroscopy study up to 100 GPa. *Phys. Chem. Miner.* **33**, 575–585. Available at: http://link.springer.com/10.1007/s00269-006-0105-y.

Lin J.-F., Speziale S., Mao Z. and Marquardt H. (2013) EFFECTS OF THE ELECTRONIC SPIN TRANSITIONS OF IRON IN LOWER MANTLE MINERALS: IMPLICATIONS FOR DEEP MANTLE GEOPHYSICS AND GEOCHEMISTRY. *Rev. Geophys.* **51**, 244–275. Available at: http://doi.wiley.com/10.1002/rog.20010.

Liu J., Dauphas N., Roskosz M., Hu M. Y., Yang H., Bi W., Zhao J., Alp E. E., Hu J. Y. and Lin J. F. (2017) Iron isotopic fractionation between silicate mantle and metallic core at high pressure. *Nat. Commun.* **8**, ncomms14377.

Liu J., Dorfman S. M., Zhu F., Li J., Wang Y., Zhang D., Xiao Y., Bi W. and Ercan Alp E. (2018) Valence and spin states of iron are invisible in Earth's lower mantle. *Nat. Commun.* **9**, 1–9. Available at: http://dx.doi.org/10.1038/s41467-018-03671-5.

881 Liu J., Mysen B., Fei Y. and Li J. (2015) Recoil-free fractions of iron in aluminous
882 bridgmanite from temperature-dependent Mössbauer spectra. *Am. Mineral.* **100**,
883 1978–1984. Available at: https://pubs.geoscienceworld.org/ammin/article/100/8-
884 9/1978-1984/106340.
885 Mao H. K., Xu J. and Bell P. M. (1986) Calibration of the ruby pressure gauge to 800
886 kbar under quasi-hydrostatic conditions. *J. Geophys. Res.* **91**, 4673. Available at:
887 http://doi.wiley.com/10.1029/JB091iB05p04673.
888 Mao Z., Lin J.-F., Liu J. and Prakapenka V. B. (2011) Thermal equation of state of
889 lower-mantle ferropericlase across the spin crossover. *Geophys. Res. Lett.* **38**,
890 n/a-n/a. Available at: http://doi.wiley.com/10.1029/2011GL049915.
891 Mao Z., Lin J. F., Yang J., Inoue T. and Prakapenka V. B. (2015) Effects of the Fe3+
892 spin transition on the equation of state of bridgmanite. *Geophys. Res. Lett.* **42**,
893 4335–4342.
894 Marquardt H., Speziale S., Reichmann H. J., Frost D. J., Schilling F. R. and Garnero
895 E. J. (2009) Elastic Shear Anisotropy of Ferropericlase in Earth's Lower Mantle.
896 *Science (80-.).* **324**, 224–226. Available at:
897 http://www.sciencemag.org/cgi/doi/10.1126/science.1169365.
898 McCammon C. (1997) Perovskite as a possible sink for ferric iron in the lower
899 mantle. *Nature* **387**, 694–696. Available at:
900 http://www.nature.com/articles/42685.
901 McDonough W. F. and Sun S. -s. (1995) The composition of the Earth. *Chem. Geol.*
902 **120**, 223–253. Available at:
903 http://linkinghub.elsevier.com/retrieve/pii/0009254194001404.
904 Núñez-Valdez M., Wu Z., Yu Y. G. and Wentzcovitch R. M. (2013) Thermal
905 elasticity of (Fe x ,Mg 1− x) 2 SiO 4 olivine and wadsleyite. *Geophys. Res. Lett.*
906 **40**, 290–294. Available at: http://doi.wiley.com/10.1002/grl.50131.
907 Núñez Valdez M., Wu Z., Yu Y. G., Revenaugh J. and Wentzcovitch R. M. (2012)
908 Thermoelastic properties of ringwoodite (Fex,Mg1-x)2SiO4: Its relationship to
909 the 520km seismic discontinuity. *Earth Planet. Sci. Lett.* **351**–**352**, 115–122.
910 Poitrasson F. (2007) Does planetary differentiation really fractionate iron isotopes?
911 *Earth Planet. Sci. Lett.* **256**, 484–492.
912 Poitrasson F., Delpech G. and Grégoire M. (2013) On the iron isotope heterogeneity
913 of lithospheric mantle xenoliths: implications for mantle metasomatism, the
914 origin of basalts and the iron isotope composition of the Earth. *Contrib. to*
915 *Mineral. Petrol.* **165**, 1243–1258. Available at:
916 http://link.springer.com/10.1007/s00410-013-0856-7.
917 Poitrasson F., Halliday A. N., Lee D. C., Levasseur S. and Teutsch N. (2004) Iron
918 isotope differences between Earth, Moon, Mars and Vesta as possible records of
919 contrasted accretion mechanisms. *Earth Planet. Sci. Lett.* **223**, 253–266.
920 Poitrasson F., Roskosz M. and Corgne A. (2009) No iron isotope fractionation
921 between molten alloys and silicate melt to 2000 °C and 7.7 GPa: Experimental
922 evidence and implications for planetary differentiation and accretion. *Earth*

Planet. Sci. Lett. **278**, 376–385. Available at: http://dx.doi.org/10.1016/j.epsl.2008.12.025.

Polyakov V. B. (2009) Equilibrium Iron Isotope Fractionation at Core-Mantle Boundary Conditions. *Science (80-.).* **323**, 912–914. Available at: http://www.sciencemag.org/cgi/doi/10.1126/science.1166329.

Qian W., Wang W., Zou F. and Wu Z. (2018) Elasticity of Orthoenstatite at High Pressure and Temperature: Implications for the Origin of Low V P / V S Zones in the Mantle Wedge. *Geophys. Res. Lett.* **45**, 665–673. Available at: http://doi.wiley.com/10.1002/2017GL075647.

Rubie D. C., Nimmo F. and Melosh H. J. (2015) Formation of the Earth's Core. In *Treatise on Geophysics* Elsevier. pp. 43–79. Available at: http://linkinghub.elsevier.com/retrieve/pii/B9780444538024001548.

Rustad J. R. and Yin Q.-Z. (2009) Iron isotope fractionation in the Earth's lower mantle. *Nat. Geosci.* **2**, 514–518. Available at: http://dx.doi.org/10.1038/ngeo546.

Schauble E. A. (2011) First-principles estimates of equilibrium magnesium isotope fractionation in silicate, oxide, carbonate and hexaaquamagnesium(2+) crystals. *Geochim. Cosmochim. Acta* **75**, 844–869. Available at: http://linkinghub.elsevier.com/retrieve/pii/S0016703710006332.

Shahar A., Schauble E. A., Caracas R., Gleason A. E., Reagan M. M., Xiao Y., Shu J. and Mao W. (2016) Pressure-dependent isotopic composition of iron alloys. *Science (80-.).* **352**, 580–582.

Shim S.-H., Grocholski B., Ye Y., Alp E. E., Xu S., Morgan D., Meng Y. and Prakapenka V. B. (2017) Stability of ferrous-iron-rich bridgmanite under reducing midmantle conditions. *Proc. Natl. Acad. Sci.* **114**, 6468–6473. Available at: http://www.pnas.org/lookup/doi/10.1073/pnas.1614036114.

Shukla G. and Wentzcovitch R. M. (2016) Spin crossover in (Mg,Fe3+)(Si,Fe3+)O3bridgmanite: Effects of disorder, iron concentration, and temperature. *Phys. Earth Planet. Inter.* **260**, 53–61. Available at: http://dx.doi.org/10.1016/j.pepi.2016.09.003.

Shukla G., Wu Z., Hsu H., Floris A., Cococcioni M. and Wentzcovitch R. M. (2015) Thermoelasticity of Fe 2+ -bearing bridgmanite. *Geophys. Res. Lett.* **42**, 1741–1749. Available at: http://doi.wiley.com/10.1002/2014GL062888.

Siebert J., Badro J., Antonangeli D. and Ryerson F. J. (2012) Metal-silicate partitioning of Ni and Co in a deep magma ocean. *Earth Planet. Sci. Lett.* **321–322**, 189–197. Available at: http://dx.doi.org/10.1016/j.epsl.2012.01.013.

Sossi P. A., Halverson G. P., Nebel O. and Eggins S. M. (2015) Combined Separation of Cu, Fe and Zn from Rock Matrices and Improved Analytical Protocols for Stable Isotope Determination. *Geostand. Geoanalytical Res.* **39**, 129–149. Available at: http://doi.wiley.com/10.1111/j.1751-908X.2014.00298.x.

Sossi P. A., Nebel O. and Foden J. (2016) Iron isotope systematics in planetary reservoirs. *Earth Planet. Sci. Lett.* **452**, 295–308. Available at:

965 http://dx.doi.org/10.1016/j.epsl.2016.07.032.
966 Teng F.-Z., Dauphas N. and Helz R. T. (2008) Iron Isotope Fractionation During
967 Magmatic Differentiation in Kilauea Iki Lava Lake. *Science (80-.).* **320**, 1620–
968 1622. Available at:
969 http://www.sciencemag.org/cgi/doi/10.1126/science.1157166.
970 Teng F.-Z., Dauphas N. and Watkins J. M. (2017) Non-Traditional Stable Isotopes:
971 Retrospective and Prospective. *Rev. Mineral. Geochemistry* **82**, 1 LP – 26.
972 Available at: http://rimg.geoscienceworld.org/content/82/1/1.abstract.
973 Teng F. Z., Dauphas N., Huang S. and Marty B. (2013) Iron isotopic systematics of
974 oceanic basalts. *Geochim. Cosmochim. Acta* **107**, 12–26. Available at:
975 http://dx.doi.org/10.1016/j.gca.2012.12.027.
976 Togo A. and Tanaka I. (2015) First principles phonon calculations in materials
977 science. *Scr. Mater.* **108**, 1–5. Available at:
978 http://dx.doi.org/10.1016/j.scriptamat.2015.07.021.
979 Vanderbilt D. (1990) Soft self-consistent pseudopotentials in a generalized eigenvalue
980 formalism. *Phys. Rev. B* **41**, 7892–7895. Available at:
981 http://link.aps.org/doi/10.1103/PhysRevB.41.7892.
982 Wang W., Qin T., Zhou C., Huang S., Wu Z. and Huang F. (2017a) Concentration
983 effect on equilibrium fractionation of Mg-Ca isotopes in carbonate minerals:
984 Insights from first-principles calculations. *Geochim. Cosmochim. Acta* **208**, 185–
985 197. Available at: http://dx.doi.org/10.1016/j.gca.2017.03.023.
986 Wang W., Walter M. J., Peng Y., Redfern S. and Wu Z. (2019a) Constraining olivine
987 abundance and water content of the mantle at the 410-km discontinuity from the
988 elasticity of olivine and wadsleyite. *Earth Planet. Sci. Lett.* **519**, 1–11. Available
989 at: https://doi.org/10.1016/j.epsl.2019.04.018.
990 Wang W. and Wu Z. (2018) Elasticity of Corundum at High Pressures and
991 Temperatures: Implications for Pyrope Decomposition and Al-Content Effect on
992 Elastic Properties of Bridgmanite. *J. Geophys. Res. Solid Earth* **123**, 1201–1216.
993 Available at: http://doi.wiley.com/10.1002/2017JB015088.
994 Wang W., Zhou C., Liu Y., Wu Z. and Huang F. (2019b) Equilibrium Mg isotope
995 fractionation among aqueous Mg2+, carbonates, brucite and lizardite: Insights
996 from first-principles molecular dynamics simulations. *Geochim. Cosmochim.*
997 *Acta* **250**, 117–129. Available at: https://doi.org/10.1016/j.gca.2019.01.042.
998 Wang W., Zhou C., Qin T., Kang J., Huang S., Wu Z. and Huang F. (2017b) Effect of
999 Ca content on equilibrium Ca isotope fractionation between orthopyroxene and
1000 clinopyroxene. *Geochim. Cosmochim. Acta* **219**, 44–56. Available at:
1001 http://dx.doi.org/10.1016/j.gca.2017.09.022.
1002 Wang X., Tsuchiya T. and Hase A. (2015) Computational support for a pyrolitic
1003 lower mantle containing ferric iron. *Nat. Geosci.* **8**, 556–559. Available at:
1004 http://www.nature.com/doifinder/10.1038/ngeo2458.
1005 Wicks J. K., Jackson J. M. and Sturhahn W. (2010) Very low sound velocities in iron-
1006 rich (Mg,Fe)O: Implications for the core-mantle boundary region. *Geophys. Res.*

Lett. **37**, n/a-n/a. Available at: http://doi.wiley.com/10.1029/2010GL043689.
Woodland A. B., Kornprobst J. and Tabit A. (2006) Ferric iron in orogenic lherzolite massifs and controls of oxygen fugacity in the upper mantle. *Lithos* **89**, 222–241.
Wu Z. (2016) Velocity structure and composition of the lower mantle with spin crossover in ferropericlase. *J. Geophys. Res. Solid Earth* **121**, 2304–2314. Available at: http://doi.wiley.com/10.1002/2015JB012667.
Wu Z., Huang F. and Huang S. (2015a) Isotope fractionation induced by phase transformation: First-principles investigation for Mg2SiO4. *Earth Planet. Sci. Lett.* **409**, 339–347. Available at: http://dx.doi.org/10.1016/j.epsl.2014.11.004.
Wu Z., Huang F. and Huang S. (2015b) Isotope fractionation induced by phase transformation: First-principles investigation for Mg2SiO4. *Earth Planet. Sci. Lett.* **409**, 339–347.
Wu Z., Justo J. F. and Wentzcovitch R. M. (2013) Elastic Anomalies in a Spin-Crossover System: Ferropericlase at Lower Mantle Conditions. *Phys. Rev. Lett.* **110**, 228501. Available at: http://link.aps.org/doi/10.1103/PhysRevLett.110.228501.
Yang H., Lin J. F., Hu M. Y., Roskosz M., Bi W., Zhao J., Alp E. E., Liu Jin, Liu Jiachao, Wentzowitch R. M., Okuchi T. and Dauphas N. (2019) Iron isotopic fractionation in mineral phases from Earth's lower mantle: Did terrestrial magma ocean crystallization fractionate iron isotopes? *Earth Planet. Sci. Lett.* **506**, 113–122. Available at: https://doi.org/10.1016/j.epsl.2018.10.034.
Yu Y. G., Hsu H., Cococcioni M. and Wentzcovitch R. M. (2012) Spin states and hyperfine interactions of iron incorporated in MgSiO3post-perovskite. *Earth Planet. Sci. Lett.* **331**–**332**, 1–7.
Zhang S., Cottaar S., Liu T., Stackhouse S. and Militzer B. (2016) High-pressure, temperature elasticity of Fe- and Al-bearing MgSiO3: Implications for the Earth's lower mantle. *Earth Planet. Sci. Lett.* **434**, 264–273. Available at: http://dx.doi.org/10.1016/j.epsl.2015.11.030.